

# Effective and Highly Selective CO Generation from CO<sub>2</sub> Using a Polycrystalline $\alpha$ -Mo<sub>2</sub>C Catalyst

Xianyun Liu,<sup>†,‡</sup> Christian Kunkel,<sup>§</sup> Pilar Ramírez de la Piscina,<sup>†</sup> Narcís Homs,<sup>\*,†,‡</sup>  
Francesc Viñes,<sup>§</sup> and Francesc Illas<sup>\*,§</sup>

<sup>†</sup>*Departament de Química Inorgànica i Orgànica, secció de Química Inorgànica, & Institut de Nanociència i Nanotecnologia (IN2UB), Universitat de Barcelona, Martí i Franquès 1, 08028 Barcelona, Spain*

<sup>‡</sup>*Catalonia Institute for Energy Research (IREC), Jardins de les Dones de Negre 1, 08930 Barcelona, Spain*

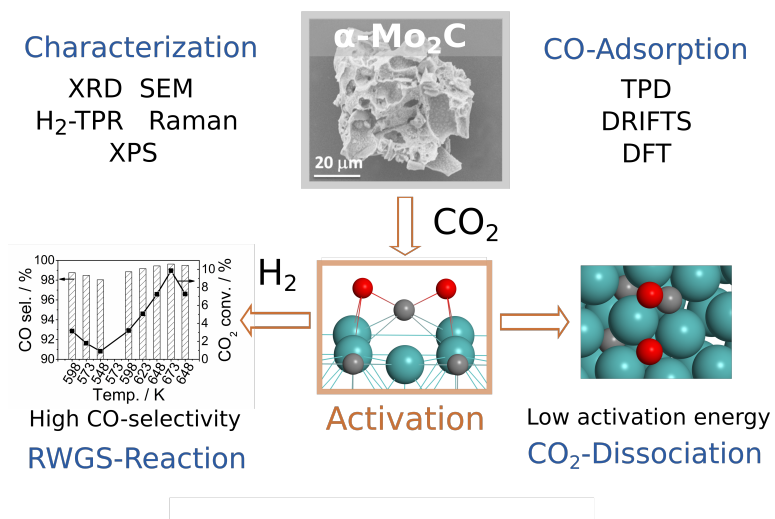
<sup>§</sup>*Departament de Ciència de Materials i Química Física & Institut de Química Teòrica i Computacional (IQTCUB), Universitat de Barcelona, Martí i Franquès 1, 08028 Barcelona, Spain*

**ABSTRACT:** Present experiments show that synthesized polycrystalline hexagonal  $\alpha$ -Mo<sub>2</sub>C is a highly efficient and selective catalyst for CO<sub>2</sub> uptake and conversion to CO through the reverse water gas shift reaction. The CO<sub>2</sub> conversion is ~16% at 673 K, with selectivity towards CO > 99%. CO<sub>2</sub> and CO adsorption is monitored by DRIFTS, TPD, and microcalorimetry, and a series of DFT based calculations including the contribution of dispersion terms. The DFT calculations on most stable model surfaces allow for identifying numerous binding sites present on the catalyst surface, leading to a high complexity in measured and interpreted IR- and TPD-spectra. The computational results also explain ambient temperature CO<sub>2</sub> dissociation towards CO as resulting from the presence of surface facets such as Mo<sub>2</sub>C(201)-Mo/C —displaying Mo and C surface atoms— and Mo-terminated Mo<sub>2</sub>C(001)-Mo. An *ab initio* thermodynamics consideration of reaction conditions however demonstrates that these facets bind CO<sub>2</sub> and CO + O intermediates too strong for a subsequent removal, whereas the Mo<sub>2</sub>C(101)-Mo/C exhibits balanced binding properties, serving a possible explanation of the observed reactivity. In summary, results show that polycrystalline  $\alpha$ -Mo<sub>2</sub>C is an economically viable, highly efficient, and selective catalyst for CO generation using CO<sub>2</sub> as a feedstock.

**Keywords:** CO<sub>2</sub> abatement • hexagonal Mo<sub>2</sub>C • CO<sub>2</sub> activation • density functional theory • reverse water gas shift

# GRAPHICAL ABSTRACT:

## EXPERIMENT AND THEORY



## INTRODUCTION

With CO<sub>2</sub> being a main active greenhouse gas in the Earth's atmosphere, there is a clear interest in its possible use of as an out-stream chemical feedstock to contribute to the reduction of its atmosphere content.<sup>1-4</sup> Alongside, CO<sub>2</sub> could be considered as a cheap carbon C<sub>1</sub> source for upgrading rather than a waste with consequences in global warming. However, the direct transformation to final sealable, added value products is rather difficult, especially at an industrial scale. This is because a possible heterogeneous catalytic conversion is hindered by the CO<sub>2</sub> high chemical stability and low chemical reactivity. Not surprisingly, there is a huge interest in finding materials which could act as appropriate and active catalysts for chemical processes involving CO<sub>2</sub>. Clearly, such a material must be capable to efficiently bind and activate CO<sub>2</sub>. One particular approach to CO<sub>2</sub> utilization is its reduction to CO employing H<sub>2</sub> as a reducing agent *via* the reverse water gas shift (RWGS) reaction:



After a RWGS step, a CO<sub>2</sub>/CO/H<sub>2</sub> out-stream mixture can be produced *via* H<sub>2</sub>O separation which can be subsequently used as syngas input for other large scale, well-established, chemical processes, such as the Fischer-Tropsch (FT) or the methanol synthesis. The RWGS reaction can be carried out under mild conditions aided by an appropriate catalyst, often a precious, expensive, scarce metal.<sup>5</sup>

Transition metal carbides (TMCs)<sup>6,7</sup> are known to display versatile catalytic properties, often described as Pt-like,<sup>7</sup> with the inherent benefit of their abundance and affordable cost. TMCs have been shown to be efficient catalysts for a handful of reactions, such as olefin isomerisation<sup>8</sup> desulfurization processes,<sup>9</sup> WGS,<sup>10</sup> and CO hydrogenation,<sup>11</sup> just to name a few. Lately, TMCs have been proposed as catalysts for CO<sub>2</sub> activation and potential materials for CO<sub>2</sub> abatement.<sup>12</sup> Among the available TMCs, orthorhombic Mo<sub>2</sub>C ( $\beta$ -Mo<sub>2</sub>C) has been proven to strongly bind and subsequently dissociate CO<sub>2</sub>, in accordance with experimental results.<sup>13,14</sup> A recent comparative study indicates that  $\beta$ -Mo<sub>2</sub>C shows high CO<sub>2</sub> conversion and CO selectivity in the RWGS, when compared with other TMCs (TM = Ti, Zr, Nb, Ta, and W).<sup>15</sup>

Motivated by these interesting catalytic properties, a number of density functional theory (DFT) computational studies have been reported involving TMCs, including methanol synthesis using  $\beta$ -Mo<sub>2</sub>C,<sup>14</sup> WGS on TiC,<sup>10</sup> H<sub>2</sub> dissociation on hexagonal Mo<sub>2</sub>C ( $\alpha$ -Mo<sub>2</sub>C)<sup>16</sup> and syngas based reactions also on  $\alpha$ -Mo<sub>2</sub>C.<sup>17</sup> Specifically relevant in the context of present work is the study of the WGS reaction on a  $\alpha$ -Mo<sub>2</sub>C(001) molybdenum terminated surface—hereafter denoted as  $\alpha$ -Mo<sub>2</sub>C(001)-Mo—by Tominaga *et al.*<sup>18</sup> who found CO<sub>2</sub> formation from adsorbed CO and O as being the rate limiting step. They also identified the CO adsorption mode comparing experimental infrared (IR) spectra with DFT results. Activation of CO<sub>2</sub> on a surface facet of  $\alpha$ -Mo<sub>2</sub>C was reported by Luo *et al.*<sup>19</sup> in the course of formic acid dissociation. Finally, Shi *et al.*<sup>20</sup> provided detailed potential energy surfaces and activation barriers for small molecules dissociation and CO<sub>2</sub> hydrogenation on the  $\alpha$ -Mo<sub>2</sub>C(101) surface, featuring both C and Mo atoms, and so denoted  $\alpha$ -Mo<sub>2</sub>C(101)-Mo/C, as well as on the  $\alpha$ -Mo<sub>2</sub>C(001)-Mo surface.

Given the results described above, it is not surprising that Mo<sub>2</sub>C based samples have been rather recently proposed as a more economic alternative to noble metals based catalysts for the RWGS reaction.<sup>21</sup> However, most experimental studies to date used single crystal surfaces and/or studied the reaction at pressures higher than atmospheric. Under these experimental conditions, besides CO, methanol and/or methane are also obtained.<sup>14</sup> The interest in designing new and performing Mo<sub>2</sub>C based catalysts for RWGS led us to deeply study CO<sub>2</sub> activation and hydrogenation over polycrystalline samples of hexagonal Mo<sub>2</sub>C ( $\alpha$ -Mo<sub>2</sub>C). Such  $\alpha$ -Mo<sub>2</sub>C samples were prepared and fully characterized and their reactivity towards CO<sub>2</sub> and their catalytic behaviour under RWGS conditions in the 548-673 K temperature range at atmospheric pressure were analyzed. Here we show that polycrystalline  $\alpha$ -Mo<sub>2</sub>C features outstanding performance, displaying high CO<sub>2</sub> conversion and selectivity for CO at mild temperatures. Results are interpreted on the basis of state-of-the-art DFT periodic calculations carried out on appropriate slab models representing the different surfaces likely to be present and highlight the great capability of  $\alpha$ -Mo<sub>2</sub>C surfaces in capturing and selectively decomposing CO<sub>2</sub> into CO.

## EXPERIMENTAL SECTION

### *Preparation of $\alpha$ -Mo<sub>2</sub>C and characterization methods.*

The  $\alpha$ -Mo<sub>2</sub>C sample was synthesized using an urea sol-gel method.<sup>22</sup> Thus, 8.2 g of urea were added to an alcoholic solution of MoCl<sub>5</sub> (urea/MoCl<sub>5</sub> = 7 mol/mol ratio) with continuous stirring until urea was completely dissolved and a viscous solution was formed. The viscous solution was treated at 333 K in air and then transferred to a quartz tube, treated under Ar flow up to 1073 K (3 K min<sup>-1</sup>). The sample was cooled under Ar flow till room temperature and then exposed to the air without passivation.

N<sub>2</sub> adsorption-desorption isotherms were recorded at 77 K using a Micromeritics Tristar II 3020 equipment. The specific surface area ( $S_{\text{BET}}$ ) was calculated by multi-point BET analysis of nitrogen adsorption isotherms. The X-ray powder diffraction (XRD) analysis was performed using a PANalytical X'Pert PRO MPD Alpha1 powder diffractometer equipped with a CuK $\alpha$ <sub>1</sub> radiation. The XRD profiles were collected between  $2\theta = 4^\circ$  and  $2\theta = 100^\circ$ , with a step width of  $0.017^\circ$  and by counting 50 s at each step. The mean crystallite sizes of  $\alpha$ -Mo<sub>2</sub>C were calculated using Debye-Scherrer equation. The morphology of the samples was observed by scanning electron microscopy (SEM) on a ZEISS Auriga equipment equipped with an energy dispersive X-ray detector (EDX).

H<sub>2</sub>-temperature programmed reduction (H<sub>2</sub>-TPR) experiments were performed using a Micromeritics AutoChem II 2920 chemisorption analyzer. After pretreatment at 363 K under He, the sample was exposed to a H<sub>2</sub>/Ar (12% v/v) flow, and the temperature was linearly increased at 10 K min<sup>-1</sup> up to 1073 K.

X-ray photoelectron spectra (XPS) were performed in a Perkin Elmer PHI-5500 Multitechnique System (Physical Electronics) with an Al X-ray source ( $h\nu = 1486.6$  eV and 350 W). All measurements were carried out in an ultra high vacuum chamber with a pressure in the  $5 \cdot 10^{-9}$ – $2 \cdot 10^{-8}$  torr range during data acquisition. The binding energy (BE) values were referred to the BE of C 1s of adventitious carbon at 284.8 eV, which was previously determined using Au as reference. Raman spectroscopy analyses were performed using a Jobin-Yvon LabRam HR 800, fitted to an optical Olympus BXFM microscope with a 532 nm laser and a CCD detector. The Raman spectra of the samples were collected with laser power limited to 1.5 mW to minimize laser-heating effects.

CO-temperature programmed desorption (CO-TPD) experiments were carried out using a Micromeritics Autochem HP 2950 instrument. Prior to CO adsorption, the sample was treated under He or under H<sub>2</sub>/Ar flow (12% v/v) at 573 K, and then cooled down to 308 K under He. The CO adsorption (10% v/v CO/He) was carried out at 308 K. The temperature programmed desorption was carried out under He flow with temperature increasing at 10 K min<sup>-1</sup> up to 1073 K.

The adsorption enthalpy of CO<sub>2</sub> was measured using a Sensys evo TG-DSC instrument (Setaram) equipped with a 3D thermal flow sensor. The α-Mo<sub>2</sub>C sample was reduced in H<sub>2</sub>/Ar (12% v/v) flow at 573 K and then cooled down to 308 K under Ar flow. After that, CO<sub>2</sub>/He (10% v/v) was flowed to the catalyst at 308 K. The exothermic peak corresponding to CO<sub>2</sub> adsorption was integrated to provide the total enthalpy of adsorption. The mean adsorption energy was calculated by considering the total amount of adsorbed CO<sub>2</sub>. The same equipment coupled to a mass spectrometer analyzer (Balzers) was used to analyze the reactivity of α-Mo<sub>2</sub>C in front of CO<sub>2</sub>.

CO<sub>2</sub> and CO adsorption was followed by *in situ* diffuse reflectance infrared spectroscopy (DRIFTS). A Bruker VERTEX 70 FTIR spectrometer equipped with a liquid nitrogen-cooled MCT detector and a Harrick Scientific HVC-DRP-4 catalytic chamber was used. The spectra recorded consisted of 256 scans at a spectral resolution of 4 cm<sup>-1</sup>. For the adsorption experiments, the sample was first treated *in situ* in the DRIFTS cell under a He flow up to 573 K, then cooled to 308 K under He. Afterwards a CO<sub>2</sub>/He (10% v/v) or CO/He (10% v/v) mixture was admitted at 308 K and contacted with the sample for 20 min. Before recording the final spectra, the sample was flushed with He and cooled to 298 K.

#### *RWGS reaction catalytic tests.*

The RWGS reaction tests were performed in a Microactivity-Reference unit (PID Eng&Tech) using a tubular fixed-bed reactor. The catalyst sample, 150 mg or 300 mg, was diluted with inactive silicon carbide up to a catalytic bed having a total volume of 1 mL. The temperature was measured by a thermocouple in direct contact with the catalyst bed. Fresh α-Mo<sub>2</sub>C was employed for reaction without any pretreatment. The sample was flowed with N<sub>2</sub> from 298 K up to 548 K and then it was exposed to a reactant gas mixture of CO<sub>2</sub>/H<sub>2</sub>/N<sub>2</sub>=1/1/3 under a gas hourly space velocity (GHSV) of 3000 h<sup>-1</sup> or 6000 h<sup>-1</sup>. The RWGS was studied between 548–673 K at 0.1 MPa. The products were analyzed on-line

with a Varian 450-GC-MS equipped with TCD, FID and mass detector. CO and CO<sub>2</sub> are separated and converted into methane using an appropriate methanizer, and then CH<sub>4</sub> formed is determined by the FID channel. CO<sub>2</sub> conversion and product distribution was determined at each temperature by the average of at least 3 different analyses.

### *Computational methods*

Periodic DFT calculations on suitable surface models (described below) have been carried out with the Vienna *ab initio* simulation package (VASP),<sup>23</sup> using the Perdew-Burke-Ernzerhof (PBE) exchange-correlation (xc) functional,<sup>24</sup> and adding the D3 dispersion contribution as proposed by Grimme (PBE-D3).<sup>25</sup> The specific settings for these computations are provided in the Supporting Information. From results of these calculations, peak desorption temperatures for adsorbed CO and IR-fingerprints of adsorbed CO and CO<sub>2</sub> have been simulated. Further, *ab initio thermodynamics* calculations for CO<sub>2</sub> adsorption and dissociation under reaction conditions have been carried out. For details on all these methods we also refer to the Supporting Information, Figure S1 and Figure S2.

### *Surface models and adsorption study*

For bulk hexagonal  $\alpha$ -Mo<sub>2</sub>C we used the eclipsed stacking mode employed previously by Shi *et al.*<sup>26</sup> A caveat is necessary here, as the other stable (orthorhombic) crystalline phase of Mo<sub>2</sub>C has been named as  $\alpha$ -Mo<sub>2</sub>C in some works in the past, and *vice versa*.<sup>26,27</sup> Bulk optimizations carried out using the PBE functional yield lattice parameters ( $a = 3.04 \text{ \AA}$ ,  $c = 4.73 \text{ \AA}$ ) in agreement with previous values and those experimentally reported.<sup>27</sup> Note that surface slabs notation follows that of Wang and coworkers and are based on their bulk unit cell definition.<sup>27</sup>

Four highly stable  $\alpha$ -Mo<sub>2</sub>C surfaces, see below for specifications, have been initially modelled using periodic (1×1) slabs with a vacuum of 10  $\text{\AA}$  inserted in the  $c$  direction, thereby avoiding interactions between translationally repeated slabs, see Figure 1. Prior to the envisioned adsorption study, bulk truncated surface slabs had been relaxed with the lower half fixed as in bulk structure to account for surface relaxations effects, see Figure 1. The results obtained from surface relaxation are in line, in terms of cleavage energy trends and geometrical structures, with those previously obtained ones by Shi *et al.*<sup>26</sup> using the revised PBE xc functional (RPBE). On the relaxed sides of the surface

models, CO<sub>2</sub> and CO adsorption was studied in a thorough systematic manner: First, non-equivalent adsorption sites for each surface were defined as in Figure 1, distinguishing between top, bridge, and hollow sites. Site notation follows that of Wang *et al.*<sup>28</sup> whenever possible; otherwise, a similar notation has been devised on previously unexplored surfaces. To investigate the possible effect of Mo oxidation state during CO adsorption, the MoO<sub>2</sub> (011) and MoO<sub>3</sub>(010) surfaces have been also studied, as detailed in the Supporting information, to provide comparison when needed (Figure S2).

Adsorption energies on these surface models have been calculated as  $E_{ads} = E_{M/slab} - (E_{slab} + E_M)$  where  $E_{M/slab}$  is the total energy of the molecule (M = CO<sub>2</sub> or CO) adsorbed on the slab,  $E_{slab}$  is the energy of the relaxed pristine slab, and  $E_M$  is the energy of the isolated gas phase molecule optimized at  $\Gamma$ -point in an asymmetric box of 9×10×11 Å dimensions. With this definition, the more negative the  $E_{ads}$ , the stronger the adsorption. All  $E_{ads}$  values include Zero Point Energy (ZPE) correction using computed harmonic frequencies. The activation energy barriers ( $E_a$ ) have been calculated as  $E_a = E_{TS} - E_{IS}$ , with  $E_{IS}$  and  $E_{TS}$  being the adsorption energies of the initial- and the previously located transition states. More details are provided in the Supporting Information.

## RESULTS AND DISCUSSION

Before entering in detail on the results, it is worth to stress out here first that the  $\alpha$ -Mo<sub>2</sub>C sample performs excellent for the RWGS: In particular, a conversion near the thermodynamic equilibrium of 16% is reached, with a selectivity towards CO versus CH<sub>4</sub> above 99.5% at 673 K and 0.1 MPa of pressure gases pressure, see below. However, to properly address and support the catalytic results, characterization and simulations are commented first, to support on them the observed catalysis.

### *Morphological, structural, and surface characterization of the synthesized polycrystalline $\alpha$ -Mo<sub>2</sub>C samples*

The preparation method used led to  $\alpha$ -Mo<sub>2</sub>C with a good crystallinity according to its XRD pattern (Figure S3); other XRD peaks than those assigned to  $\alpha$ -Mo<sub>2</sub>C (JCPDS 00-035-0787) were not found. The crystallite size of the hexagonal  $\alpha$ -Mo<sub>2</sub>C, calculated using the Scherrer equation and the (101) peak, was found to be 35.2 nm. The BET surface area

of the sample was  $7.7 \text{ m}^2 \text{ g}^{-1}$ . SEM analysis of the prepared  $\alpha\text{-Mo}_2\text{C}$  showed aggregates containing rough and smooth parts (Figure S4). The EDX analysis (mapping images in Figure S4) indicated the presence of Mo, C, and O; the presence of oxygen is tentatively assigned to the presence of surface molybdenum oxide and/or oxycarbide species formed during the preparation of the sample and/or when the  $\alpha\text{-Mo}_2\text{C}$  is exposed to the air. For  $\text{Mo}_2\text{C}$  freshly prepared by carburization, the surface oxidation by oxygen,  $\text{CO}_2$ , or  $\text{H}_2\text{O}$  has been deeply studied by *in situ* FTIR spectroscopy.<sup>29,30</sup> It has been proposed that a thin layer of protective oxycarbide is formed when mild oxidants such as  $\text{CO}_2$  or  $\text{H}_2\text{O}$  are used; the extent of surface oxidation when  $\text{O}_2$  is used for passivation is more difficult to control.

In order to check the presence of surface molybdenum oxides and/or residual amorphous carbon, we have examined the fresh  $\alpha\text{-Mo}_2\text{C}$  sample in different zones by Raman spectroscopy (see Figure S5a). Only in some cases, very low intensity bands at  $\sim 1350 \text{ cm}^{-1}$  and  $\sim 1580 \text{ cm}^{-1}$  (D and G bands), were detected, indicating that negligible contents of carbonaceous residues would be present in the synthesized  $\alpha\text{-Mo}_2\text{C}$ . Although the Raman spectrum in the zone  $100\text{-}1000 \text{ cm}^{-1}$  is complex, it points to the presence of different surface molybdenum oxide species, such as  $\text{MoO}_3$  and other intermediate oxides  $\text{MoO}_{3-x}$  (Figure S5a).<sup>31</sup> This is further confirmed by XPS; Figure 2a shows the corresponding Mo 3d XPS peak, which can be deconvoluted into four (Mo  $3d_{5/2}$ , Mo  $3d_{3/2}$ ) doublets. Peaks at (233.2 eV, 236.3 eV), (232.1 eV, 235.2 eV) and (230.0 eV, 232.9 eV) are assigned to  $\text{Mo}^{6+}$ ,  $\text{Mo}^{5+}$  and  $\text{Mo}^{4+}$  surface species, respectively.<sup>21,32</sup> The (228.8 eV, 231.9 eV) doublet could be related to the presence of  $\text{Mo}^{2+}$  and/or  $\text{Mo}^{3+}$ , which could be ascribed to  $\text{Mo}_2\text{C}$  and/or oxycarbide species.<sup>21,33</sup> The corresponding O 1s XPS peak with a maximum at 531.1 eV (Figure S6a) is broad and asymmetric, and can be reasonably assigned to  $\text{O}^{2-}$  bonded to  $\text{Mo}^{n+}$  in oxide and oxycarbide species;<sup>21,34,35</sup> the shoulder at high BE values can be indicative of the presence of oxygen in C-O and C=O species.<sup>21,33,35,36</sup> The C 1s peak can be deconvoluted into four components at 283.8 eV, 284.8 eV, 286.0 eV, and 288.7 eV, (Figure S7a), which can be assigned to C-Mo, C-C, C-O and O=C-O species, respectively.<sup>33,35-38</sup>

Finally, Figure 3 shows the  $\text{H}_2$ -TPR profile of the sample; the main peak at 554 K can be assigned to the reduction of molybdenum oxycarbide.<sup>39</sup> The reduction of surface molybdenum oxides could account for the  $\text{H}_2$  consumption at temperatures higher than 590

K. The reduction of  $\text{MoO}_3$  is known to take place through different intermediate species towards  $\text{MoO}_2$ , and the reduction of  $\text{MoO}_2$  to  $\text{Mo}$  is expected at temperatures above 800 K.<sup>40</sup>

*Probing the  $\alpha\text{-Mo}_2\text{C}$  samples through CO adsorption: DRIFTS and TPD measurements and DFT calculations*

From the above-presented experimental results, the presence of *a)* bare  $\alpha\text{-Mo}_2\text{C}$  surfaces on the fresh sample is confirmed with parts possibly covered by *b)* oxycarbide species. Further, *c)* some molybdenum oxides  $\text{MoO}_{3-x}$  could be present. In the following we use CO adsorption as a probe, to establish model surfaces for cases *a-c)*, able to capture the experimental samples behaviour arriving at a sample description with regard to its exposed active sites. The analysis is carried out on the basis of CO-DRIFTS and CO-TPD experiments, interpreted from results of periodic DFT calculations. For convenience, the computational results on CO adsorption are presented first and we will refer to the different surfaces by the corresponding Miller indexes only, omitting the chemical formula.

CO adsorption on *a)* bare  $\alpha\text{-Mo}_2\text{C}$  surfaces, has previously been theoretically studied on the (101)-Mo/C, (001)-Mo, and (201)-Mo/C surfaces, yet not addressing the vibrational fingerprints.<sup>28</sup> As far as the (001)-C termination is concerned, Han *et al.*<sup>41,42</sup> described CO adsorption on its reconstructed surface. Shi and coworkers exhaustively studied CO adsorption and dissociation on (001)-Mo and (001)-C surfaces, accounting for vibrational frequencies, yet employing a cluster model.<sup>43</sup> Still, key information for our analysis was missing and we therefore conducted a systematic and complete study. The results of the DFT based calculations for CO adsorbed on the different  $\alpha\text{-Mo}_2\text{C}$  surfaces are listed in Table 1 and the optimized geometries are depicted in Figure S8. In short, CO chemisorption on all studied surfaces involves a considerable number of binding sites. For most stable sites, CO  $E_{ads}$  values of -1.48 eV on (101)-Mo/C, -2.87 eV on (201)-Mo/C, -2.67 eV on (001)-Mo, and -1.88 eV on (001)-C surfaces are found at the PBE level, increased by 0.15-0.24 eV when including dispersion contributions using the PBE-D3 method. Thus, CO adsorption mostly stems out from an electronic effect. The (001)-C surface is to be discussed apart as exposes surface C atoms to which CO binds, forming a  $\text{C}=\text{C}=\text{O}$  species (ketenylidene). Apart from bulk terminated (001)-C surface, we also considered the reconstructed (001)-C surface shown in Figure S1. Here, ketenylidene

species are also formed on top of two non-equivalent surface carbons (Figure S1 and Table 2).

We considered also the influence of *b*) oxycarbide species in two ways: First, single oxygen adatoms could alter the chemical properties of active sites on  $\alpha$ -Mo<sub>2</sub>C surface: An oxygen adatom adsorbed vicinal to CO would then likely exert the greatest effect. DFT-results for such cases are presented in Table 3 and, except in the case of the (001)-C surface, indicate a weakening of CO binding relative to the respective cases for adsorption at bare surfaces, see Table 1. A slight alteration of adsorbate geometry is further caused; still, these CO adsorption sites are not deactivated, indicating that a focus on the bare  $\alpha$ -Mo<sub>2</sub>C surfaces provides a fairly well description of active sites on the sample. Apart, parts of  $\alpha$ -Mo<sub>2</sub>C surfaces are likely covered with a full oxygen monolayer, found in theoretical studies to be the most stable situation on surfaces of  $\beta$ -Mo<sub>2</sub>C<sup>44,45</sup> and  $\alpha$ -Mo<sub>2</sub>C,<sup>46</sup> while medium coverage situations were considered to be of less importance. Liu *et al.*<sup>44</sup> demonstrated that a monolayer oxygen coverage effectively deactivates (001)-Mo and (001)-C  $\beta$ -Mo<sub>2</sub>C surfaces ( $\alpha$ -Mo<sub>2</sub>C in their notation), rendering CO and CO<sub>2</sub> adsorption unfavorable. A similar effect is to be expected from oxygen covered  $\alpha$ -Mo<sub>2</sub>C surfaces and, for the oncoming discussion, we thus omit the influence of such oxycarbides on adsorption.

Finally, since *c*) molybdenum oxides MoO<sub>3-x</sub> also possibly coordinate CO, we modelled CO adsorption on MoO<sub>2</sub> and MoO<sub>3</sub> surfaces thereby considering Mo<sup>4+</sup> and Mo<sup>6+</sup> sites. Note that MoO<sub>2</sub> was also detected by XRD (Figure S3) in the sample after a CO<sub>2</sub> treatment at 673 K. There are seldom reports theoretically studying MoO<sub>2</sub>, however some model surfaces have been described by Tokarz-Sobieraj *et al.*<sup>47</sup> Following their work we found considerably stable CO adsorption on MoO<sub>2</sub> (011) surface with adsorption energies of -1.19 (-1.39) and -0.98 (-1.18) eV, respectively obtained at PBE (PBE-D3) level (Table 2). Here, CO is coordinated perpendicularly on top of Mo-atoms, see Figure S2a. Finally, CO interaction with studied surfaces of MoO<sub>3</sub> was found to be weak, see Figure S2b. Interaction is here ascribable to physisorption in accordance with experimental results,<sup>48</sup> at ambient temperatures likely favouring desorption. We therefore discarded MoO<sub>3</sub> from further discussion.

From previous discussion, possible adsorption sites are known and located on  $\alpha$ -Mo<sub>2</sub>C and MoO<sub>2</sub> surfaces. Considering *in situ* CO adsorption studied by DRIFTS, Figure 4

shows the spectrum in the 2250-1250  $\text{cm}^{-1}$  region. Notice how most significant features are located below 2000  $\text{cm}^{-1}$ , yet weak broad bands centred at 2163  $\text{cm}^{-1}$  and 2063  $\text{cm}^{-1}$  are also clearly visible. CO species linearly coordinated to surface  $\text{Mo}^{n+}$  oxide species are expected to give rise to  $\nu_{\text{CO}}$  bands above 2000  $\text{cm}^{-1}$ . From existing literature, CO coordinated to  $\text{Mo}^{5+}$  sites could contribute to the band centred at 2163  $\text{cm}^{-1}$ ; a band at 2183  $\text{cm}^{-1}$  has been proposed due to the coordination of CO on  $\text{Mo}^{5+}$  sites.<sup>49</sup> However, present calculations link the band at 2163  $\text{cm}^{-1}$  to C=C=O species formed on the unreconstructed (001)-C surface. To further support this assignment we note that on the unreconstructed (001)-C surface  $\nu_{\text{CO}}$  is predicted to appear at 2142  $\text{cm}^{-1}$  whereas accounting for reconstruction frequencies slightly shifts this value to 2110  $\text{cm}^{-1}$  and 2118  $\text{cm}^{-1}$  (Table 2). Thus, reconstruction does not seem to lead to a significantly different signature. Alternatively, what seems a determining factor is the coupling with surface phonons; on the reconstructed (001)-C surface, Han *et al.*<sup>41</sup> published a CO stretching value decoupled from the surface of 2066  $\text{cm}^{-1}$ , which we could reproduce likewise to 2071  $\text{cm}^{-1}$ , and so, phonon coupling enlarges the stretching by 39 to 47  $\text{cm}^{-1}$ . Note that a band at 2196  $\text{cm}^{-1}$  has been related to ketene species for the  $\text{Mo}_2\text{C}/\text{Al}_2\text{O}_3$  supported system.<sup>29</sup> From previous work, the broad band centred at 2063  $\text{cm}^{-1}$  could be attributed to the coordination of CO on surface  $\text{Mo}^{n+}$  sites ( $n < 4$ ), likely molybdenum oxycarbide species. This is supported from experiments regarding the  $\text{Mo}_2\text{C}/\text{Al}_2\text{O}_3$  system exhibiting characteristic bands at 2054  $\text{cm}^{-1}$  and 2081  $\text{cm}^{-1}$  attributed to  $\text{Mo}^{m+}$  and  $\text{Mo}^{k+}$  sites, where  $0 < m < 2 < k < 3$ .<sup>30</sup> Present model calculations (Table 2) suggest that the band at 2031  $\text{cm}^{-1}$  is likely to be due to CO adsorption on  $\text{MoO}_2$  (011). It is worth noting that the suggested assignments are based on considering an overall accuracy of  $\pm 35 \text{ cm}^{-1}$  with anharmonicity and coverage effects being the main sources of disagreement.

The IR spectrum in Figure 4 features main bands below 2000  $\text{cm}^{-1}$ . The theoretical calculations relate the bands with maxima at 1919, 1827, 1772, 1747, 1647, and 1585  $\text{cm}^{-1}$  to the stretching modes of CO adsorbed on the (201)-Mo/C terminated surface. To provide a complete overview, possible assignments based on the calculated vibrational frequencies reported in Table 1 and Table 2 are summarized in Table 4. The values at 1772  $\text{cm}^{-1}$  and 1747  $\text{cm}^{-1}$  can be easily explained based on symmetric and asymmetric coupling of adsorbed vicinal CO groups. Likewise the bands at 1507, 1458, and 1415  $\text{cm}^{-1}$  could be

attributed to CO adsorbed on (001)-Mo and (001)-C terminated surfaces. Despite a quantitative determination from the DRIFTS experiment is challenging, the high population of CO on (201)-Mo/C and (001)-Mo surfaces linked to the strongest adsorption, see above, could account for the intensity of the observed infrared bands measured at 308 K. The band at  $1993\text{ cm}^{-1}$  could be related to CO adsorbed on (001)-C (T1 site) and/or (101)-Mo/C (T2 site) and that at  $1945\text{ cm}^{-1}$  to CO on (101)-Mo/C (T4 site) and/or (001)-C (T2 site) surfaces. Finally, we note that other peaks present in the spectrum cannot be unambiguously assigned, *e.g.* it is hard to assign the feature at  $1699\text{ cm}^{-1}$  on the basis of the present model calculations only. The presence of defects, CO adsorption on other non-contemplated less-stable surfaces or alterations in vibrational frequency induced by neighbouring oxygen adatoms (see again Table 3) can account for the appearance of such bands.

Further analysis is gained by TPD experiments, see Figure 5. The CO adsorption carried out at 308 K onto the catalyst previously treated at 573 K with either He or 12% H<sub>2</sub>/Ar flow at 573 K, delivers similar profiles, and only that of the H<sub>2</sub>-treated  $\alpha$ -Mo<sub>2</sub>C is shown. A total adsorption of 0.24 mmol CO/g was determined, and CO desorption started at 323 K achieving a first relative maximum at around 415 K, then increased up to 463 K, and from this temperature desorption profiles slowly decreased. The experimental TPD profile points to the presence of different adsorption sites with different adsorption energies; the higher the CO desorption temperature is, the stronger is the CO interaction with the surface, with a concomitant larger adsorption energy. To further confirm the present assignments, Figure 5 includes the experimental TPD profile and desorption peak temperatures calculated from the present theoretical models (see Tables 1 and 2). The simulation has been carried out for each of the identified minimum energy structures and using a similar approach to that applied and discussed in detail elsewhere.<sup>50-52</sup> Note that adsorption energies from PBE-D3 were used, as dispersion terms noticeably contribute to the strength of binding to the catalyst surface. The comparison in Figure 5 shows that the observed broad temperature range for CO desorption is indeed explainable as consisting of superimposed desorption peaks from numerous exposed CO binding sites. Further the magnitude of the adsorption interaction in different temperature regions can now be used to approximately estimate the quantity of exposed surfaces. From qualitative comparison, experimental peaks of highest intensity at 415 K and 463 K could originate from desorption

from the most stable and therefore likely most exposed (101)-Mo/C surface, thus further supporting the assignment. Further, the (001)-C surface could play a role in the desorption region below 600 K, whereas the desorption above 600 K could be related with higher adsorption energy sites as found on (201)-Mo/C and (001)-Mo terminations. The desorption peaks associated to MoO<sub>2</sub> which are expected below 400 K are also included in Figure 5. Last, note that slight disagreements in TPD can be tracked back to exposure of other minority surfaces, here not contemplated, by the presence of oxygen adatoms lowering adsorption strengths (see again Table 3) and can further be related to coverage effects during desorption, as demonstrated by Wang *et al.*<sup>28</sup> Moreover, note that, as stated above, the adsorption energies have been evaluated at coverages of  $1/4$  to  $1/8$  ML, likely to represent a realistic approximate coverage at a peak desorption rate.

#### *CO<sub>2</sub> adsorption studied by DRIFTS, microcalorimetry, and DFT*

The theoretical modelling of CO<sub>2</sub> adsorption has been carried out following the strategy employed to study CO adsorption. The DFT based calculations for CO<sub>2</sub> on well-defined  $\alpha$ -Mo<sub>2</sub>C surfaces are used to guide the assignment of spectroscopic features measured on the synthesized samples. Again, many possible adsorption sites with high adsorption energy (Table 5) were found for CO<sub>2</sub> interacting with the four surfaces considered in the present work (Figure 1). Moreover, in the course of geometry optimization an easy CO<sub>2</sub> dissociation with C-O bond scission was often found. Table 6 shows the initial position of CO<sub>2</sub> and the final position of CO and O when geometry optimization indicated a CO<sub>2</sub> spontaneous dissociation where we ascertain a presumably small energy barrier. Figures S9 and S10 in the supporting information, show the adsorbate geometries for molecular and dissociative CO<sub>2</sub> adsorptions, respectively. Briefly, on the most stable surface (101)-Mo/C surface, adsorption energies for T3 and B2 of -0.86 and -0.85 eV, respectively, compare well to values of -0.87 (-0.92) and -0.81 (-0.81) eV found by Luo *et al.* for  $1/4$  ML ( $1/16$  ML).<sup>19</sup> For H4 on (001)-Mo, a previous adsorption energy of -1.70 (-2.07) eV for PBE (-D3)<sup>20</sup> compares well to a value of -1.78 (-2.09) eV reported here. Our results show that, similarly to CO, adsorption energies on (001)-Mo and (201)-Mo/C are considerably higher than those on (101)-Mo/C and (001)-C surfaces. Again, PBE-D3 values of adsorption energy were only 0.26-0.34 eV higher than PBE values, whereas geometries are similar, indicating that adsorption and CO<sub>2</sub> activation is largely of chemical

(electronic) origin. In general, the adsorbed CO<sub>2</sub> species are bent with  $\alpha(\text{OCO})$  angles between 116.4° and 136.8° and C-O bond lengths in the range 1.18-1.48 Å. In each case at least one of the two C-O bond is significantly enlarged compared to the gas phase value of  $d(\text{C-O}) = 1.177$  Å. Both findings strongly indicate CO<sub>2</sub> activation by charge transfer from the underlying surface, as previously observed on other TMCs.<sup>12</sup> In some cases the lengthening of the two C-O bonds differs considerably indicating a preferential C-O scission.

We determined the transition states for those systems where spontaneous CO<sub>2</sub> dissociation was observed during molecular adsorption. Thus, CO<sub>2</sub><sup>δ-</sup> most stable adsorbed situations were identified and the transition state along the pathway. This was carried out for the four surfaces at PBE-D3 level, starting from most stable adsorption geometry of CO<sub>2</sub> and going to CO + O final states in Table 3. Results are summarized in Figure 6. Activation energies from the CO<sub>2</sub><sup>δ-</sup> towards CO + O reveal significant reactivity differences between the different studied surfaces. On (101)-Mo/C starting from B2 site, and from TC on (001)-C surfaces, C-O bond scission implies activation energies of 0.59 and 0.63 eV, respectively. In contrast, lower activation energies of 0.26 and 0.32 eV are predicted from H3 on (201)-Mo/C and from H4 on (001)-Mo. Note here, that for (001)-Mo an effective barrier is given with the low energy pathway consisting of a conversion from H4 to H4 (3) by torsional motion and a subsequent C-O bond scission. A previously reported activation barrier of 0.69 eV on (101)-Mo/C is in full agreement with present results, whereas the value of 0.56 eV reported on (001)-Mo is reproduced as 0.54 eV when dissociation is directly contemplated from H4.<sup>20</sup> All in all present theoretical results indicate a high CO<sub>2</sub> uptake with subsequent activation and decomposition into CO at low temperature likely to occur on (201)-Mo/C and (001)-Mo surfaces, as well as the high temperature opening of the CO<sub>2</sub> dissociation channel on (101)-Mo/C and (001)-C surfaces.

To gain a first insight on which surface ending could actively catalyse the CO<sub>2</sub> dissociation step, *ab initio atomistic thermodynamics*<sup>53</sup> was employed, allowing for a consideration of RWGS reaction conditions. Note that these conditions are approximated by a temperature of  $T = 600$  K and steady-state partial pressures of  $p_{\text{CO}_2} = p_{\text{H}_2} = 0.2$  bar for CO<sub>2(g)}</sub> and H<sub>2(g)}</sub> and  $p_{\text{H}_2\text{O}} = p_{\text{CO}} = 1$  mbar for CO<sub>(g)}</sub> and H<sub>2</sub>O<sub>(g)}</sub>. Respective Gibbs free energy profiles for CO<sub>2</sub> adsorption, dissociation to adsorbed CO + O, subsequent

hydrogenation and removal as  $\text{CO}_{(\text{g})} + \text{H}_2\text{O}_{(\text{g})}$  are given in Figure 6; transition states have been included for the purpose of visualization. According to the results, dissociation to  $\text{CO} + \text{O}$  is the most favourable state on all tested surface facets, and considering the kinetic evidence presented before, this state can likely be reached in all cases. A subsequent removal of  $\text{CO}$  and  $\text{O}$  however only seems viable on the (101)-Mo/C surface, where  $\Delta G_{\text{ads}}$  for  $\text{CO} + \text{O} + \text{H}_2_{(\text{g})}$  and for  $\text{CO}_{(\text{g})} + \text{H}_2\text{O}_{(\text{g})}$  are in a similar range with  $-0.58$  eV and  $-0.37$  eV respectively. Given the results presented above, the inclusion of nearby oxygen adatoms, could even modulate this energetic situation favourably. Note also, that the further dissociation of  $\text{CO}$  to  $\text{C} + \text{O}$  was found to be slightly less favourable ( $-0.23$  eV). In contrast to the situation found for (101)-Mo/C, dissociation to  $\text{CO} + \text{O}$  on (201)-Mo/C, (001)-Mo and (001)-C is considerably more exergonic and intermediates are then likely bound too strongly for an efficient reaction to occur and we thus here neglect a possible further dissociation of the adsorbed  $\text{CO}$ , together with the experimental evidence of the lack of oxycarbide formation. In total, the thermodynamic analysis suggests occurrence of the RWGS on the most stable (101)-Mo/C, providing a possible explanation for the RWGS reactivity detailed below, but with a full mechanistic investigation being out of the scope of the current work.

The vibrational fingerprints of the above commented adsorption conformations are summarized in Table 5, which contains the two highest frequencies  $\nu_1$  and  $\nu_2$ , which from analysis of the normal modes correspond to symmetric and asymmetric stretching of the bent adsorbed  $\text{CO}_2$  molecule. Figure 4 compares the experimental DRIFT spectrum obtained after  $\text{CO}_2$  adsorption and simulated IR spectrum of adsorbed  $\text{CO}_2$ . The many features exhibited by the experimental spectrum can be interpreted on the light of the spectrum obtained after  $\text{CO}$  adsorption and with the support of the simulated IR of adsorbed  $\text{CO}$  and  $\text{CO}_2$  chemisorption on the different  $\alpha\text{-Mo}_2\text{C}$  surfaces. Notice, for instance, that bands above  $2000\text{ cm}^{-1}$  were already present after  $\text{CO}$  adsorption, and related to ketenylidene species on (001)-C surface and  $\text{CO}$  adsorbed on surface  $\text{Mo}^{\text{n+}}$  sites. Indeed fingerprints of molecularly adsorbed  $\text{CO}_2$  do not appear at frequencies higher than  $1800\text{ cm}^{-1}$  (Table 5). This implies that some  $\text{CO}_2$  molecules dissociated at the experimental temperature of  $308\text{ K}$ . It is worth to note the different position and relative intensity of these high frequency bands when dosing  $\text{CO}_2$ ; the  $\text{O}$  adatoms generated during the  $\text{CO}_2$

treatment can modify the vibrational frequency of the CO fragments, take *e.g.* the differences between  $\nu(\text{CO})$  for respective cases found in Tables 1 and 3. For instance, the strong band around  $1895\text{ cm}^{-1}$  can be assigned to CO adsorption on the T3 site of (101)-Mo/C (Table 1) when influenced by the effect of O adatom(s), now visible due to the overall lower intensity, and thus supporting the exposure of most stable (101)-Mo/C surface. As stated above,  $\text{CO}_2$  related spectrum shows up in the  $2000\text{-}1000\text{ cm}^{-1}$  region. The spectrum complexity prevents a straightforward unambiguous assignment. However, simulated IR predicts that  $\text{CO}_2$  adsorbed on different  $\alpha\text{-Mo}_2\text{C}$  surfaces would rise  $\nu_1(\text{CO}_2)$  and  $\nu_2(\text{CO}_2)$  bands in the  $1800\text{-}1200\text{ cm}^{-1}$  range and  $1300\text{-}700\text{ cm}^{-1}$  range, respectively (Table 5). However,  $\nu(\text{CO})$  bands generated from adsorbed CO resulting from  $\text{CO}_2$  scission are expected to appear in the same region. Indeed, main bands at  $1690\text{ cm}^{-1}$  and  $1594\text{ cm}^{-1}$  could be also contributed by adsorbed CO on  $\alpha\text{-Mo}_2\text{C}$ . Added complexity in the  $1500\text{-}1300\text{ cm}^{-1}$  region could come from  $\text{CO}_2$  adsorbed on (001)-Mo. Below  $1300\text{ cm}^{-1}$  contribution from all studied surfaces is possible and one should refrain from a more detailed assignment. Still, the wealth of observed peaks in both our DRIFT studies suggest that a mere focus on most stable adsorption could here lead to an incomplete description, being more complete when other situations close in energy are considered, probably reachable under reaction conditions, or prompted by coverage or surface point defect effects.

For a better quantitative analysis of the adsorption of  $\text{CO}_2$  on the  $\alpha\text{-Mo}_2\text{C}$  catalyst,  $\text{CO}_2$  adsorption was followed by microcalorimetry. The mean  $\text{CO}_2$  adsorption heat determined for the sample was  $-3.2\text{ eV}$ , similar in magnitude to the calculated final states for  $\text{CO} + \text{O}$  on (201)-Mo/C or (001)-Mo surfaces, with PBE-D3 energies of  $-3.62\text{ eV}$  and  $-3.90\text{ eV}$ , respectively (Figure 6). Note that the experimental heat has to be regarded as an average involving different situations, including  $\text{CO}_2$  non-dissociative adsorption, and  $\text{CO}_2$  decomposition on other surfaces as well, yet present results strongly suggest adsorption of  $\text{CO} + \text{O}$  as a main ruler.

The apparent easiness of  $\text{CO}_2$  dissociation on the  $\alpha\text{-Mo}_2\text{C}$  sample leads us to further study its reactivity through different experiments. For such purpose a fresh  $\alpha\text{-Mo}_2\text{C}$  was treated with  $\text{CO}_2$  flow at  $673\text{ K}$  by  $10\text{ h}$  and then characterized. During the  $\text{CO}_2$  treatment, CO was detected in the effluent. The BET surface area of  $\alpha\text{-Mo}_2\text{C}$  determined after the  $\text{CO}_2$  treatment was  $8.3\text{ m}^2\text{ g}^{-1}$ , which is very similar to that of the fresh sample ( $7.2\text{ m}^2\text{ g}^{-1}$ ). The

corresponding XRD pattern, shown in Figure S3, indicates the presence of  $\alpha$ -Mo<sub>2</sub>C and monoclinic MoO<sub>2</sub> (JCPDS: 00-032-0671). The Raman spectrum shows bands at 740, 589, 570, 495, 457, 227, 202, and 138 cm<sup>-1</sup> assigned to the presence of MoO<sub>2</sub> patches in the sample resulting from the reaction with atomic O available at the surface from CO<sub>2</sub> dissociation (Figure S5b).<sup>31</sup> The analysis by XPS also indicates a transformation of the surface of fresh  $\alpha$ -Mo<sub>2</sub>C after the CO<sub>2</sub> treatment. Figure 2 compares the Mo 3d core level spectrum of the  $\alpha$ -Mo<sub>2</sub>C before (spectrum a) and after the CO<sub>2</sub> treatment (spectrum b). After the CO<sub>2</sub> treatment at 673 K, the Mo 3d<sub>5/2</sub> component at 229.8 eV is assigned to Mo<sup>4+</sup> species, in accordance to XRD and Raman results. After the CO<sub>2</sub> treatment, a H<sub>2</sub>-TPR experiment was carried out (Figure 3). The H<sub>2</sub>-consumption peak observed at about 544 K is related with the reduction of oxycarbide species as previously discussed. A main peak at 906 K is ascribed to the MoO<sub>2</sub> reduction.<sup>40</sup> After the H<sub>2</sub>-TPR experiment up to 1073 K, XRD peaks due to MoO<sub>2</sub> were not present; the presence of crystalline  $\alpha$ -Mo<sub>2</sub>C and Mo was determined (Figure S3).

*Catalytic behaviour of polycrystalline  $\alpha$ -Mo<sub>2</sub>C under reverse water gas shift reaction conditions.*

The RWGS reaction over the fresh  $\alpha$ -Mo<sub>2</sub>C and over a previously CO<sub>2</sub>-treated sample was studied between 548 K and 673 K under different gas hourly space velocity (GHSV) at 0.1 MPa. Under the reaction conditions used the main product found was CO; only very small amounts of CH<sub>4</sub> were detected as a function of the temperature. Figure 7 shows the catalytic behaviour as a function of the reaction temperature of the fresh  $\alpha$ -Mo<sub>2</sub>C sample. The CO<sub>2</sub> conversion increases with temperature, reaching about 16% at 673 K, a value not too far from that expected from the thermodynamic equilibrium at this temperature (*ca.* 22%). CO selectivity at 548 K was 97.5% and slightly increases, reaching 99.5% at the highest temperature studied (673 K); only very low amounts of CH<sub>4</sub> by-product were found, which decreased with increasing temperature. For CO production, apparent activation energy of  $0.57 \pm 0.02$  eV was deduced from the Arrhenius plot at the low temperature region (548-598 K) (Figure S11); this value is close to the calculated energy barriers for CO<sub>2</sub> dissociation (Figure 6). After 3h under reaction at 673 K, the contact time of reactants was decreased; Figure 8 shows the CO<sub>2</sub> conversion and the CO selectivity variation. At 673 K under a GHSV of 6000 h<sup>-1</sup>, a decrease on the CO<sub>2</sub>

conversion to 13.5% was observed; however, selectivity towards CO approached 100% under these conditions. The generation of CO is related to an easy CO<sub>2</sub> dissociation on the  $\alpha$ -Mo<sub>2</sub>C catalyst. As stated above, in a separate experiment, a fresh  $\alpha$ -Mo<sub>2</sub>C sample was previously treated with CO<sub>2</sub> at 673 K for 22 h. During the CO<sub>2</sub> treatment, CO was detected in the effluent; its concentration decreased with time. Then, the RWGS reaction under a GHSV of 3000 h<sup>-1</sup> was followed at the same temperature of 673 K. Figure 8 shows that a drastic decrease on the CO<sub>2</sub> conversion occurred meanwhile keeping the high selectivity towards CO. As discussed in the previous section, the CO<sub>2</sub> treatment at 673 K produces a partial transformation of the fresh  $\alpha$ -Mo<sub>2</sub>C resulting in the formation of MoO<sub>2</sub> species. The presence of H<sub>2</sub> under the RWGS reaction at 673 K could be able to reduce the oxycarbide species present but not the MoO<sub>2</sub>. Thus, the number of active surface centres decreased but the selectivity towards CO was maintained above 99%.

In order to verify the stability of the  $\alpha$ -Mo<sub>2</sub>C catalyst under the RWGS reaction conditions used, a new experiment was carried out. In this case, the RWGS was studied between 548 K and 673 K at 0.1 MPa using 150 mg of fresh  $\alpha$ -Mo<sub>2</sub>C catalyst under a GHSV of 3000 h<sup>-1</sup> and according to the following reaction temperature sequence: 598 K (3h) → 573 K (3h) → 548 K (10h) → 598 K (3h) → 623 K (3h) → 648 K (3h) → 673 K (3h) → 648 K (3h). In this way, the changes of catalytic behaviour of  $\alpha$ -Mo<sub>2</sub>C could be observed by changes on the CO<sub>2</sub> conversion and/or selectivity towards CO. Figure 9 shows the CO<sub>2</sub> conversion and selectivity towards CO as a function of the reaction temperature of the fresh  $\alpha$ -Mo<sub>2</sub>C sample subjected to this reaction procedure. The CO<sub>2</sub> conversion values corresponded well with those expected using less amount of catalyst and its variation with temperature, as well as that of selectivity towards CO, resulted similar to those previously found. It is worth of mention that CO<sub>2</sub> conversion and CO selectivity obtained at 598 K and 648 K did not change along the reaction sequence used.

#### *Characterization of post-RWGS catalyst.*

The post-reaction catalyst showed a BET surface area of 11.6 m<sup>2</sup> g<sup>-1</sup> close to that of the fresh  $\alpha$ -Mo<sub>2</sub>C sample (7.7 m<sup>2</sup> g<sup>-1</sup>). SEM images of the sample after RWGS reaction showed no big changes on the morphology of the sample (Figure S12). The XRD pattern of post-reaction  $\alpha$ -Mo<sub>2</sub>C (Figure S3) is similar to that of the fresh sample, indicating the only presence of crystalline hexagonal  $\alpha$ -Mo<sub>2</sub>C with a crystallite size determined by the Scherrer

equation of 35.5 nm. The registered Raman spectrum (Figure S5c) is also similar to that above discussed corresponding to the fresh  $\alpha$ -Mo<sub>2</sub>C and pointing to the presence of MoO<sub>x</sub> species. The XPS analysis of the post-RWGS yields no significant differences in the Mo 3*d* spectrum when post-reaction sample (Figure 2c) is compared with the fresh sample (Figure 2a). However, some differences are found in the O 1*s* and C 1*s* XPS signals; the presence of a greater amount of C-O and C=O surface species in post-RWGS can be proposed, see Figures S6c and S7c.

## CONCLUSIONS

The experimental results show that the prepared polycrystalline hexagonal  $\alpha$ -Mo<sub>2</sub>C is a highly efficient and highly selective catalyst for CO<sub>2</sub> uptake and conversion to CO through the reverse water gas shift reaction; from a CO<sub>2</sub>/H<sub>2</sub> = 1/1 reaction mixture, a CO<sub>2</sub> conversion of about 16% with CO selectivity of 99.5% was achieved at 673 K.

Different experimental techniques have been applied to characterize the samples and to investigate CO and CO<sub>2</sub> adsorption, and subsequent reactivity towards the reverse water gas shift reaction. The different characterization techniques reveal the expected complexity of the polycrystalline  $\alpha$ -Mo<sub>2</sub>C. However, the complex experimental behavior has been successfully interpreted from periodic DFT based calculations employing a realistic combination of most stable  $\alpha$ -Mo<sub>2</sub>C surfaces. This strategy allowed us to identify numerous binding sites and adsorption modes, as well as interpreting almost all experimental IR fingerprints and TPD desorption profiles. At this respect, our experiments indicate the formation of CO when CO<sub>2</sub> contacts with the  $\alpha$ -Mo<sub>2</sub>C catalyst even at a quite low temperature (308 K) which is consistent with calculated low energy barriers on (201)-Mo/C and (001)-Mo surfaces. The DFT results are consistent with the final state energies of -3.2 eV obtained from experimentally measured heat of adsorption of CO<sub>2</sub> on the polycrystalline  $\alpha$ -Mo<sub>2</sub>C samples. Moreover, a further presence of (101)-Mo/C and (001)-C surface facets is indirectly evidenced from experiments.

From the experimental evidence, surface oxygen increases with the CO<sub>2</sub> treatments, however, as the RWGS reaction proceeds without a decrease in conversion, continuous O removal is suggested by reduction with hydrogen under H<sub>2</sub>O formation; on the contemplated surfaces, H<sub>2</sub> could be easily adsorbed and dissociated.

A consideration of the thermodynamic situation under RWGS reaction conditions indicates that (201)-Mo/C, (001)-Mo and (001)-C surfaces could bind adsorbates too strongly not allowing for facile release or removal. In contrast, from the *ab initio* thermodynamics analysis of CO<sub>2</sub> dissociation, the (101)-Mo/C seemed to exhibit more balanced properties, activating CO<sub>2</sub> well towards dissociation, while a subsequent release of CO seems viable from a thermodynamic point of view. A presence of this surface on the catalyst can therefore provide an explanation for the observed RWGS reactivity. It is further noticeable that computed energy barriers for CO<sub>2</sub> dissociation on these surfaces are

of the same order as experimentally determined for the RWGS from Arrhenius plots at the lower temperature regime.

To summarize, polycrystalline hexagonal  $\alpha$ -Mo<sub>2</sub>C could be considered as an economically viable, highly efficient and selective catalyst for CO generation from CO<sub>2</sub> through the reverse water gas shift reaction.

## **ASSOCIATED CONTENT**

### **Supporting information**

The Supporting Information is available free of charge on the ACS Publications website at DOI: 10.1021/XXXX.XXXXXXXXXX.

Additional details related to the computational methods, surface models and adsorption modes, CO<sub>2</sub> dissociation profiles, harmonic vibrational frequencies, peak desorption temperatures and *ab initio thermodynamics* for CO<sub>2</sub> adsorption and dissociation and, data.

Detailed experimental characterization for different samples of polycrystalline  $\alpha$ -Mo<sub>2</sub>C: XRD patterns for fresh, CO<sub>2</sub> treated, H<sub>2</sub> reduced and post-RWGS sample. SEM and EDX analysis (Mo, C, O) for fresh and post-RWGS sample. Raman and XPS (O 1s and C 1s) spectra for fresh, CO<sub>2</sub> treated and post-RWGS sample. Arrhenius plot for CO production under RWGS reaction conditions.

Graphical depiction of slab models for MoO<sub>2</sub> (011), and reconstructed  $\alpha$ -Mo<sub>2</sub>C (001)-C surfaces. Geometries of stable CO and CO<sub>2</sub> adsorptions and spontaneous CO<sub>2</sub> dissociation on the contemplated surfaces. Energy diagrams for alternative pathways of CO<sub>2</sub> dissociation.

## **AUTHOR INFORMATION**

### **Corresponding Authors**

\*narcis.homs@qi.ub.edu, \*francesc.illas@ub.edu

## ACKNOWLEDEMENTS

It is to highlight that X.L and C.K. equally contributed to present work. N.H, P.R.P, and X.L. are grateful to the projects Consolider *Ingenio* 2010, Multicat CSD2009-00050 and MAT2014-52416-P for financial support. X.L. thanks the China Scholarship Council and the University of Barcelona (IN2UB) for her PhD grants. C.K, F.V, and F.I. work has been supported by Spanish MINECO/FEDER CTQ2015-64618-R grant and, in part, by *Generalitat de Catalunya* grants 2014SGR97 and XRQTC, and by European Union's Horizon 2020 research and innovation programme under grant agreement No 676580 (NOMAD). F.V. thanks MINECO for a *Ramón y Cajal* (RyC) research contract (RYC-2012-10129). F.I. acknowledges additional support from the 2015 ICREA Academia Award for Excellence in University Research. Computational time at the *Calendula* supercomputer has been provided by the Supercomputing Center Foundation of Castilla y León (FCSCL) through a grant from Red Española de Supercomputación (RES).

**Table 1.** Adsorption energy ( $E_{\text{ads}}$ , in eV), desorption temperature ( $T_{\text{d}}$ , in K), vibrational frequency of CO ( $\nu_{\text{CO}}$ , in  $\text{cm}^{-1}$ ) and its relative intensity (Rel. int.) for CO adsorbed on the different studied  $\alpha\text{-Mo}_2\text{C}$  surfaces as predicted from DFT based calculations at the PBE and (PBE-D3) level. Adsorbate geometries are given in the Figure S8, Supporting Information. Bold sites are those considered most stable. Notation of adsorption sites is as in Figure 1.

Surface	Site	$E_{\text{ads}}$	$T_{\text{d}}$	$\nu_{\text{CO}}$ (Rel.int.)
<b>(101)-Mo/C</b>	T2	-0.94 (-1.14)	285 (330)	1971 (0.59)
	T3	-1.22 (-1.43)	355 (400)	1900 (0.50)
	<b>T4</b>	<b>-1.48 (-1.66)</b>	<b>435 (470)</b>	<b>1960 (0.84)</b>
<b>(201)-Mo/C</b>	H4	-1.29 (-1.49)	330 (370)	1003 (0.02)
	T3	-1.59 (-1.78)	455 (505)	1908 (0.65)
	<b>H3</b>	<b>-2.87 (-3.10)</b>	<b>745 (800)</b>	<b>1085 (0.01)</b>
	H4	-2.02 (-2.22)	550 (605)	1614 (0.28)
	B1	-1.88 (-2.10)	525 (585)	1746 (0.26)
	B6	-2.11 (-2.31)	595 (650)	1870 (0.47)
<b>(001)-Mo</b>	B6(2)	-2.06 (-2.27)	560 (615)	1587 (0.24)
	<b>H1</b>	<b>-2.67 (-2.89)</b>	<b>720 (760)</b>	<b>1377 (0.01)</b>
	<b>H1(2)</b>	<b>-2.57 (-2.81)</b>	<b>695 (740)</b>	<b>1340 (0.01)</b>
	H2	-2.42 (-2.63)	680 (695)	1247 (0.01)
	H3	-1.91 (-2.13)	510 (565)	1433 (0.01)
	H3(2)	-1.96 (-2.16)	530 (580)	1417 (0.01)
	H4	-2.52 (-2.73)	665 (715)	1412 (0.01)
	H4(2)	-2.41 (-2.61)	650 (695)	1471 (0.02)
	B4	-2.47 (-2.69)	670 (725)	1600 (0.05)
<b>(001)-C</b>	<b>T1</b>	<b>-1.52 (-1.74)</b>	<b>430 (490)</b>	<b>1988 (0.49)</b>
	T2	-1.10 (-1.31)	310 (365)	1960 (0.37)
	<b>TC</b>	<b>-1.59 (-1.74)</b>	<b>440 (505)<sup>a</sup></b>	<b>2142 (1.00)<sup>d</sup></b> <b>1275 (0.01)<sup>b</sup></b>
	<b>H1</b>	<b>-1.88 (-2.06)</b>	<b>540 (590)<sup>a</sup></b>	<b>1477 (0.02)<sup>d</sup></b> <b>963 (0.01)<sup>b</sup></b>

<sup>a</sup> The desorption prefactor of  $10^{16} \text{ s}^{-1}$  was used. <sup>b</sup> Concerted modes of the formed C-C-O species.

**Table 2.** Adsorption energy ( $E_{\text{ads}}$ , in eV), desorption temperature ( $T_{\text{d}}$ , in K) and vibrational frequency of CO ( $\nu_{\text{CO}}$ , in  $\text{cm}^{-1}$ ) on the additionally studied surfaces as predicted from DFT based calculations at the PBE and (PBE-D3) level. The normal mode vibrational frequency for the C-O stretch is listed together to its associated relative intensity (Rel. int.). Adsorbate geometries are given in the Supporting Information. Bold sites are those considered most stable. Notation of adsorption sites is as in Figure 1.

Surface	Site	$E_{\text{ads}}$	$T_{\text{d}}$	$\nu_{\text{CO}}$ (Rel.int.)
$\alpha$ -Mo <sub>2</sub> C (001)-C reconstructed	T1	-1.62	477 <sup>a</sup>	2118 (1.00) <sup>d</sup> 1243 (0.02) <sup>b</sup>
	<b>T2</b>	<b>-1.98</b>	<b>575<sup>a</sup></b>	<b>2110 (1.00)<sup>d</sup></b> <b>1254 (0.01)<sup>b</sup></b>
MoO <sub>2</sub> (011)	T3	-1.47	395	1981 (0.51)
	T8	-0.98 (-1.18)	285 (345)	2036 (0.66)
	<b>T9</b>	<b>-1.19 (-1.39)</b>	<b>340 (395)</b>	<b>2031 (0.75)</b>

<sup>a</sup> The desorption prefactor of  $10^{16} \text{ s}^{-1}$  was used. <sup>b</sup> Concerted modes of the formed C-C-O species.

**Table 3.** Influence of vicinal O on CO adsorption exemplified for one case each on the different studied  $\alpha$ -Mo<sub>2</sub>C surfaces. Given are the final positions of CO and O together with CO adsorption energy ( $E_{\text{ads}}$ , in eV), vibrational frequency of CO ( $\nu_{\text{CO}}$ , in cm<sup>-1</sup>) and CO desorption temperature ( $T_{\text{d}}$ , in K) from DFT based calculations at the PBE and (PBE-D3) level. Notation for adsorption sites is as in Figure 1 and structures are similar to CO + O final states from Figure 6.

Surface	CO final site	O final site	$E_{\text{ads}}$	$\nu_{\text{CO}}$ (Rel.int.)	$T_{\text{d}}$
<b>(101)-Mo/C</b>	<b>T4</b>	<b>T4</b>	-1.40 (-1.60)	2016 (0.60)	400 (450)
<b>(201)-Mo/C</b>	<b>H3</b>	<b>H3</b>	-2.01 (-2.25)	1094 (0.02)	525 (580)
<b>(001)-Mo</b>	<b>H1</b>	<b>H1</b>	-2.00 (-2.21)	1502 (0.05)	535 (585)
<b>(001)-C</b>	<b>TC</b>	<b>H2</b>	-1.79 (-1.97)	2147 <sup>b</sup> (0.89) 1254 <sup>b</sup> (0.01)	530 <sup>a</sup> (575 <sup>a</sup> )

<sup>a</sup>The desorption prefactor of  $10^{16} \text{ s}^{-1}$ . <sup>b</sup>Concerted modes of the formed C-C-O

**Table 4.** Tentative assignment of the experimental values of CO related vibrational frequencies (DRIFTS). All values are in  $\text{cm}^{-1}$ . Notation of adsorption sites is as in Figure 1.

Surface	Site	Calculated	Experimental
(001)-C)	TC	2142	2163
	T1	2118	
	T2	2110	
(011) MoO <sub>2</sub>	T9	2031	2063
	T8	2036	
(001)-C	T1	1988	1993
(101)-Mo/C	T2	1971	
(101)-Mo/C	T4	1960	1945
(001)-Mo	T2	1960	
(201)-Mo/C	T3	1908	1919
(101)-Mo/C	T3	1900	
(201)-Mo/C	B6	1870	1827
(201)-Mo/C	B1	1746	1747, 1772
—			1699
(201)-Mo/C	H4	1614	1647
(001)-Mo	B4	1600	
(201)-Mo/C	B6 (2)	1587	1585
(001)-C	H1	1477	1458, 1507
(001)-Mo	H4 (2)	1471	1458, 1507
(001)-Mo	H3	1433	1415
(001)-Mo	H3 (2)	1417	
(001)-Mo	H4	1412	

**Table 5.** PBE and (PBE-D3) adsorption energy values ( $E_{\text{ads}}$ , in eV) and Gibbs free energy of adsorption ( $G_{\text{ads}}$ , in eV) at reaction conditions ( $T = 600$  K, 0.2 bar), adsorbate related highest vibrational frequencies ( $\nu_1$  and  $\nu_2$  in  $\text{cm}^{-1}$ ) and relative intensities (Rel. int.) for the stable structures of  $\text{CO}_2$  adsorbed on the different studied surfaces. Most stable sites on each surface are highlighted in bold. Site notation is as in Figure 1.

Surface	Site	$E_{\text{ads}}$	$\nu_1$ (Rel. int.)	$\nu_2$ (Rel. int.)
<b>(101)-Mo/C</b>	T1	-0.37 (-0.63)	1271 (0.00)	1160 (0.02)
	<b>T3</b>	<b>-0.86 (-1.17)</b>	<b>1515 (0.01)</b>	<b>1256 (0.02)</b>
	T3 (2)	-0.58 (-0.88)	1677 (0.05)	928 (0.01)
<b>(201)-Mo/C</b>	<b>B2</b>	<b>-0.85 (-1.11)</b>	<b>1679 (0.01)</b>	<b>1180 (0.05)</b>
	H1	-0.98 (-1.29)	1202 (0.00)	1033 (0.03)
	H1 (2)	-0.73 (-1.04)	1132 (0.01)	1064 (0.02)
	H1 (3)	-0.56 (-0.85)	1681 (0.30)	741 (0.05)
	H2	-1.14 (-1.44)	1228 (0.01)	1059 (0.03)
	H2 (2)	-1.10 (-1.39)	1565 (0.04)	1103 (0.10)
	<b>H3</b>	<b>-2.12 (-2.45)</b>	<b>1203 (0.00)</b>	<b>936 (0.06)</b>
	<b>H3 (2)</b>	<b>-2.10 (-2.42)</b>	<b>1226 (0.03)</b>	<b>874 (0.01)</b>
	<b>H3 (3)</b>	<b>-1.78 (-2.10)</b>	<b>1270 (0.02)</b>	<b>973 (0.06)</b>
	H4	-1.40 (-1.72)	1222 (0.00)	1089 (0.03)
	H4 (2)	-1.18 (-1.49)	1599 (0.28)	729 (0.11)
	H5	-0.74 (-1.06)	1538 (0.10)	899 (0.05)
	B5	-1.49 (-1.78)	1624 (0.00)	1166 (0.12)
	B6	-1.39 (-1.69)	1643 (0.00)	1167 (0.10)
	B7	-1.35 (-1.66)	1216 (0.01)	937 (0.03)
B8	-1.01 (-1.30)	1626 (0.01)	1155 (0.11)	
<b>(001)-Mo</b>	H1	-1.75 (-2.09)	1437 (0.03)	1058 (0.06)
	H1 (2)	-1.50 (-1.83)	1351 (0.02)	985 (0.04)
	H2	-1.78 (-2.11)	1243 (0.04)	857 (0.01)
	H3	-1.17 (-1.48)	1204 (0.01)	1027 (0.03)
	H3 (2)	-1.21 (-1.52)	1508 (0.02)	1074 (0.09)
	<b>H4</b>	<b>-1.78 (-2.09)</b>	<b>1116 (0.00)</b>	<b>1039 (0.30)</b>
	<b>H4 (2)</b>	<b>-1.57 (-1.89)</b>	<b>1395 (0.02)</b>	<b>986 (0.04)</b>
	<b>H4 (3)</b>	<b>-1.65 (-1.96)</b>	<b>1271 (0.00)</b>	<b>1160 (0.02)</b>
	B1	-1.46 (-1.76)	1619 (0.00)	1153 (0.10)
B2	-1.36 (-1.67)	1605 (0.00)	1150 (0.09)	
B4	-1.51 (-1.82)	1590 (0.00)	1152 (0.09)	
<b>(001)-C</b>	<b>TC</b>	<b>-0.79 (-1.06)</b>	<b>1732 (0.27)</b>	<b>970 (0.04)</b>
	TC (2)	-0.55 (-0.82)	1791 (0.39)	1020 (0.01)
	TC (3)	-0.60 (-0.86)	1749 (0.31)	962 (0.01)

**Table 6.** Adsorption of CO<sub>2</sub> naturally evolving to CO + O in the course of geometry optimization. The PBE and (PBE-D3) calculated E<sub>ads</sub> are given (eV), as well as the initial positions of CO<sub>2</sub> and the final positions of CO and O. Notation for adsorption sites is as in Figure 1 and structures are reported in Figure S10 (Supporting Information).

Surface	CO <sub>2</sub> placement	E <sub>ads</sub>	CO final site	O final site
<b>(101)-Mo/C</b>	----- Not observed -----			
<b>(201)-Mo/C</b>	T3	-2.87 (-3.18)	T3	H3
	T4	-2.90 (-3.22)	B8	H3
<b>(001)-Mo</b>	T1	-3.15 (-3.49)	H2	H4
	H2	-3.66 (-4.02)	H1(2)	H1
<b>(001)-C</b>	B1	-1.26 (-1.54)	TC	TC
	T2	-1.51 (-1.84)	H1	T1 <sup>a</sup>

<sup>a</sup>Formation of CO species with surface carbon and displacement to T1 site.

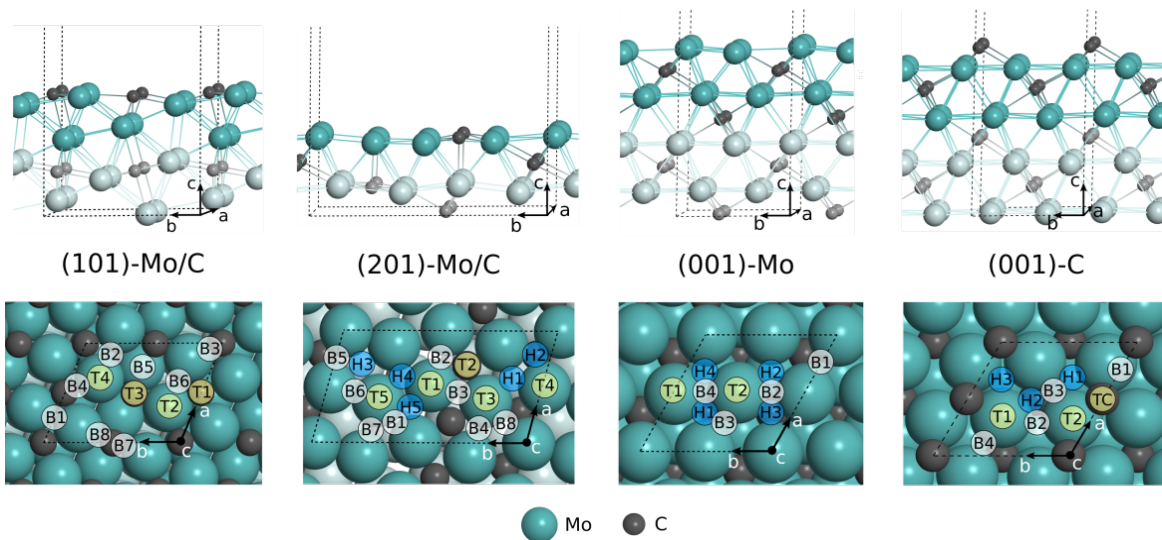


**Figure 1.** Slab models of the different bare, relaxed  $\alpha$ - $\text{Mo}_2\text{C}$  surfaces used to represent the exposed facets of the catalyst. Each model is shown in, side (top part) and top (bottom part) views. Layers in lighter colour were fixed during optimizations and frequency calculations. Non-equivalent top (T), bridge (B), and hollow (H) sites for  $\text{CO}_2$  and CO adsorption are highlighted.

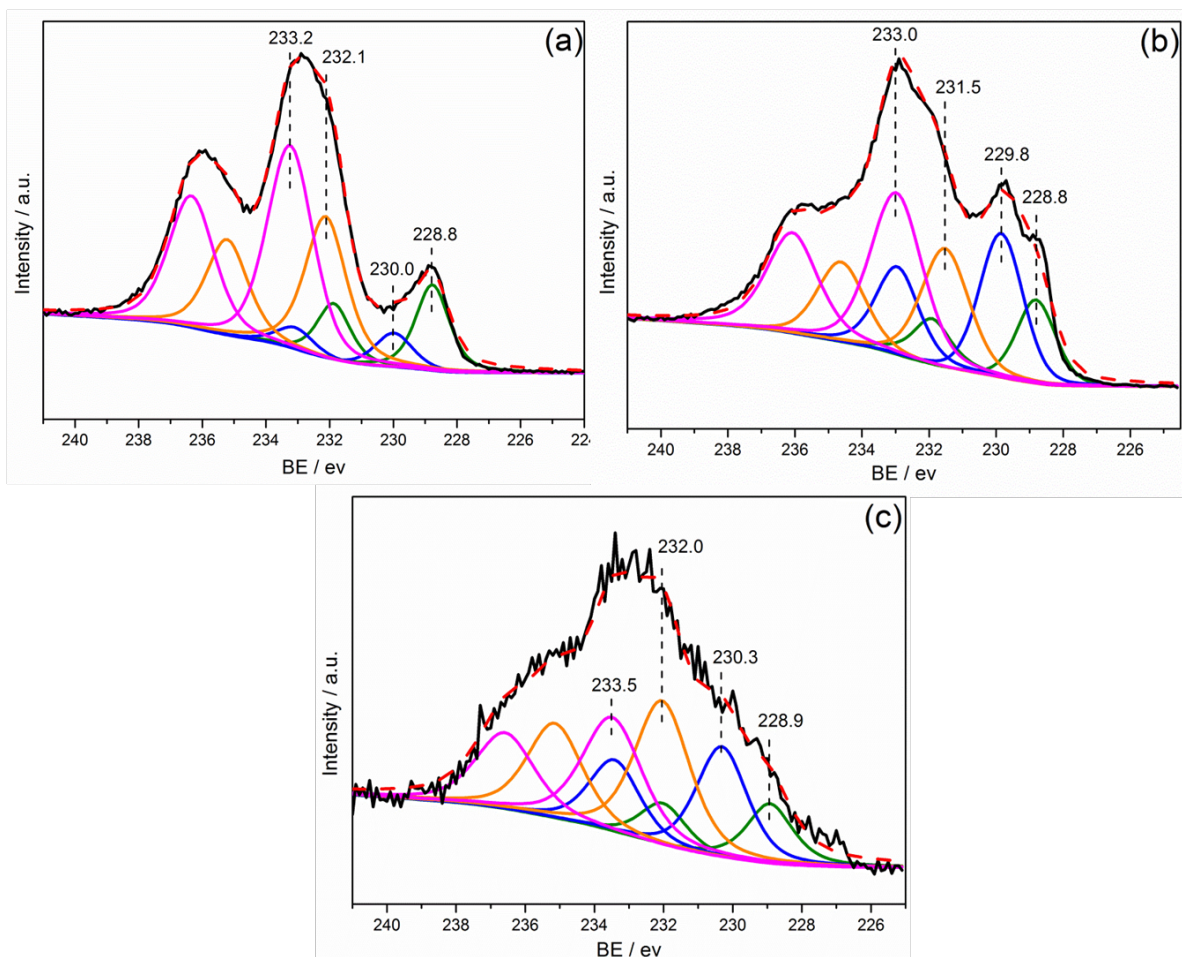


**Figure 2.** Mo 3d level XPS of  $\alpha$ -Mo<sub>2</sub>C sample: (a), fresh; (b), CO<sub>2</sub> treated at 673 K for 10 h; (c), Post-RWGS.

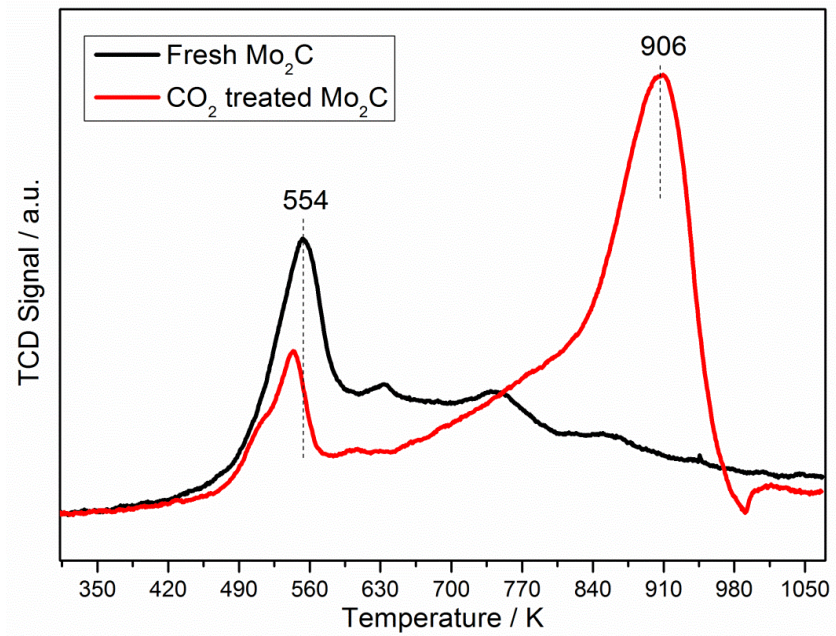


**Figure 3.** H<sub>2</sub>-TPR profiles of fresh and CO<sub>2</sub> treated (673 K, 10 h)  $\alpha$ -Mo<sub>2</sub>C

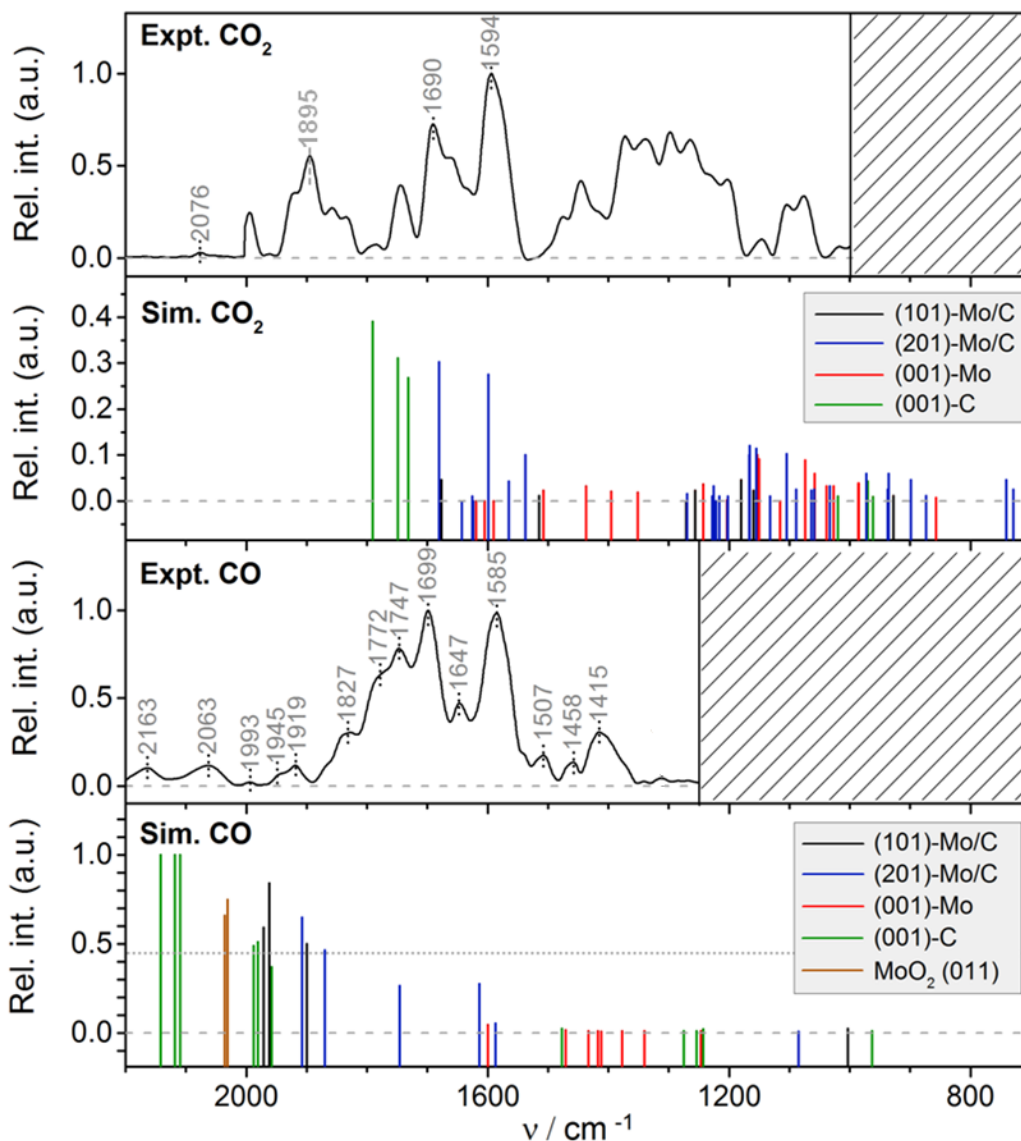


**Figure 4.** Experimental DRIFT spectra from CO<sub>2</sub> and CO adsorption and simulated infrared spectra. Experimental spectra (Expt.) have been normalized to unity for each separate case. Vertical lines in simulated infrared spectra (Sim.) correspond to vibrational wavenumbers and relative intensities (Rel. int.) as given in Tables 1, 2 and 4. Dotted grey line inserted in the simulated CO infrared graph corresponds to maximum intensity in simulated CO<sub>2</sub> infrared plot. In simulated infrared spectra, intensity scale starts below zero to depict bands with no change in perpendicular component of the dipole moment.

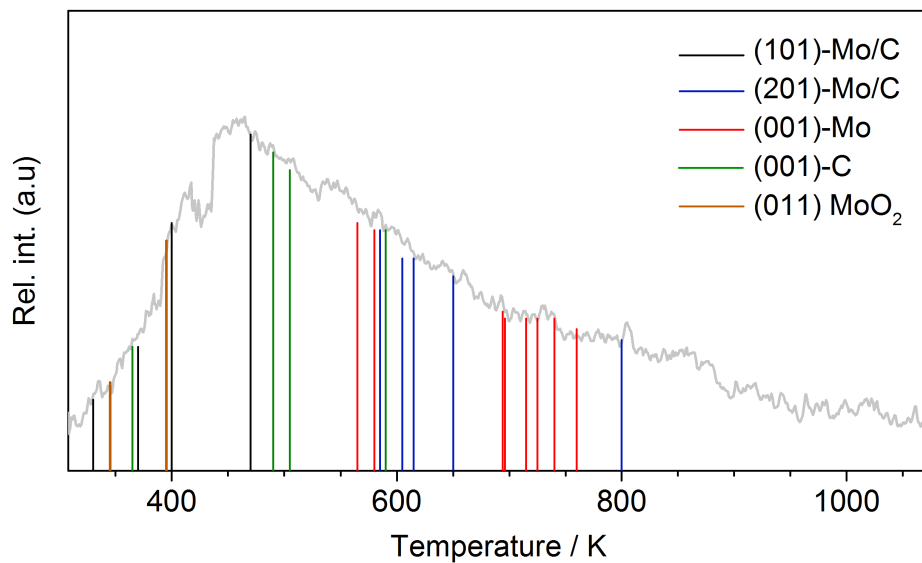


**Figure 5.** Experimental CO TPD profile (grey line) and calculated temperatures of adsorption modes corresponding to highest desorption rate (vertical colour-coded lines) as obtained from PBE-D3 values in Table 1. Note that simulated intensities have been deliberately placed to guide the eye in the comparison with the experimental profile.

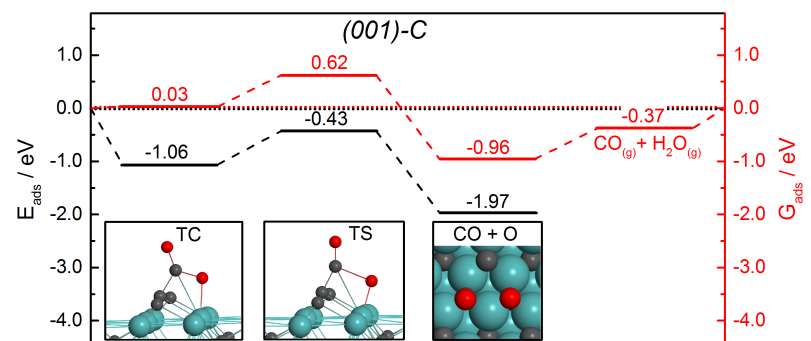
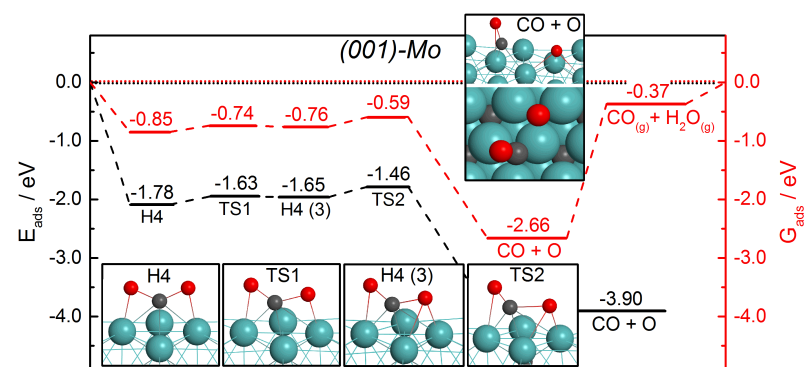
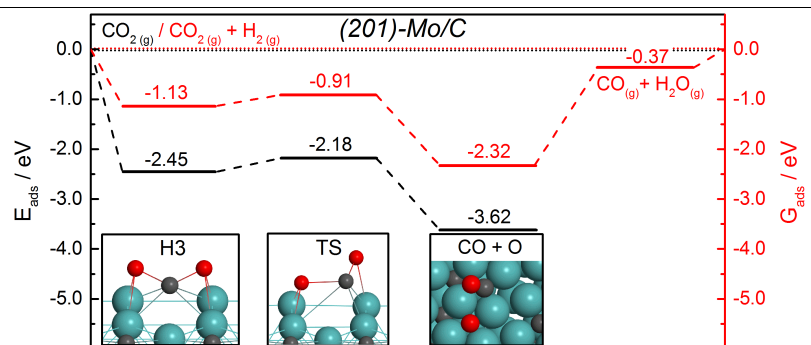
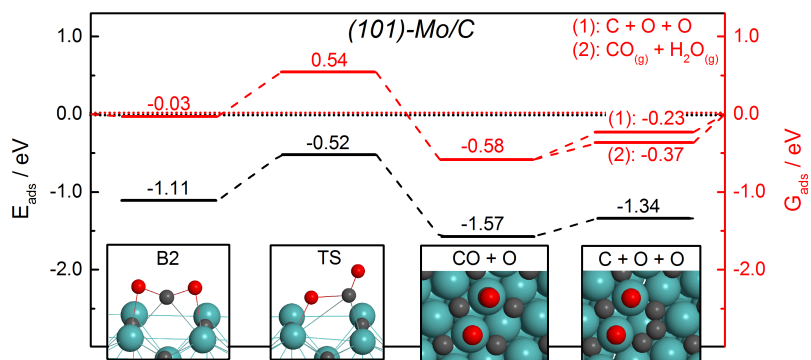


**Figure 6.** Potential energy surfaces (black) and Gibbs free energy surfaces (red, for conditions see text), of CO<sub>2</sub> dissociation to CO+O from most stable sites on different surfaces (PBE-D3 values). The zero of energy for all has been chosen as indicated in the second subplot.

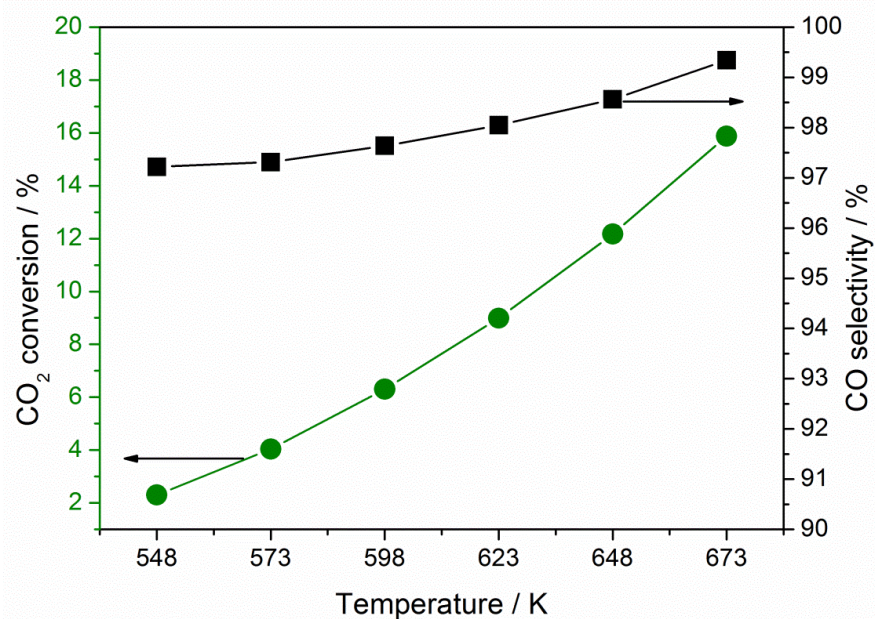


**Figure 7.** Catalytic behaviour of  $\alpha$ -Mo<sub>2</sub>C in the reverse water gas shift reaction; CO<sub>2</sub> conversion and CO selectivity, as function of reaction temperature. Reaction conditions: 300 mg catalyst, CO<sub>2</sub>/H<sub>2</sub>/N<sub>2</sub> = 1/1/3, GHSV = 3000 h<sup>-1</sup>, T = 548-673 K, P = 0.1 MPa.

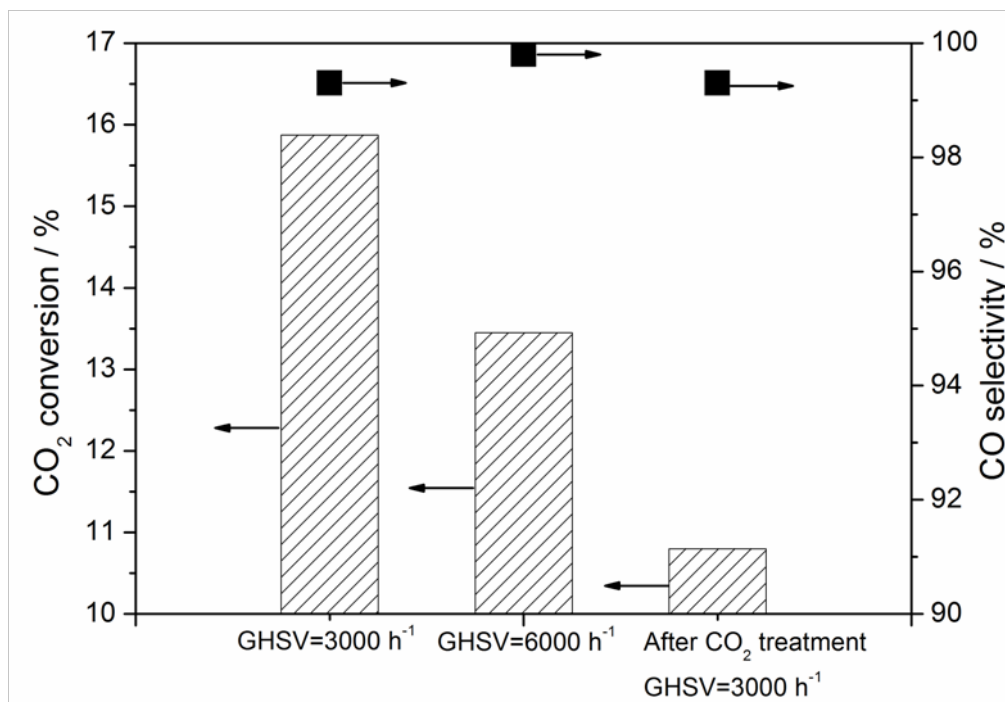


**Figure 8.** CO<sub>2</sub> conversion and CO selectivity under reverse water gas shift reaction at different contact time (GHSV) conditions of fresh and CO<sub>2</sub> treated (673 K, 10 h)  $\alpha$ -Mo<sub>2</sub>C. Reaction conditions: 300 mg catalyst, CO<sub>2</sub>/H<sub>2</sub>/N<sub>2</sub> = 1/1/3, T = 673 K, P = 0.1 MPa.

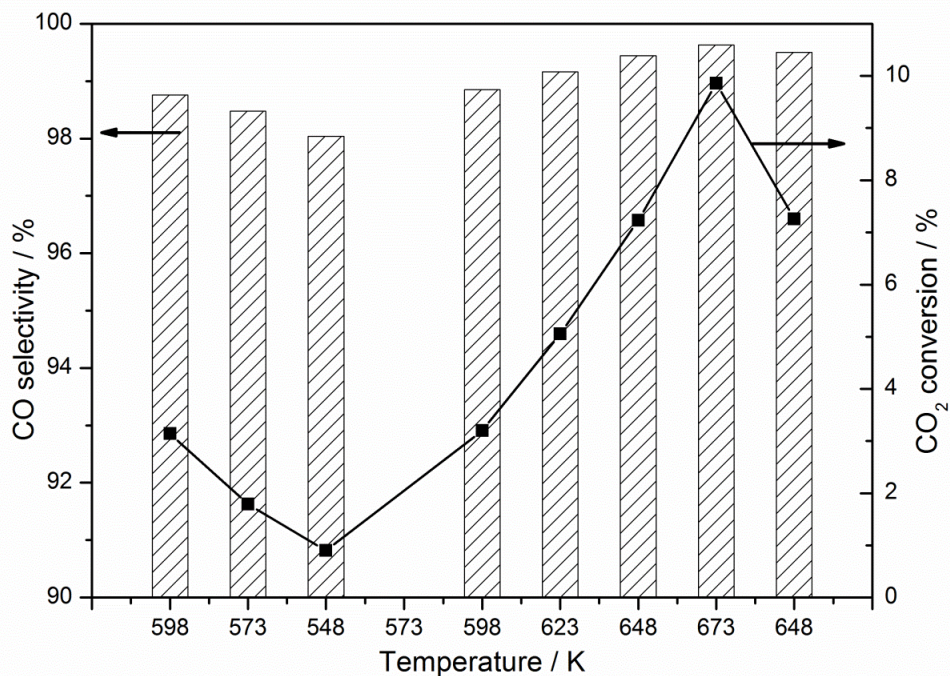


**Figure 9.** Catalytic behavior of  $\alpha$ -Mo<sub>2</sub>C in the RWGS reaction; CO<sub>2</sub> conversion and CO selectivity as function of reaction temperature using a sequential reaction temperature cycle. Reaction conditions: 150 mg catalyst, CO<sub>2</sub>/H<sub>2</sub>/N<sub>2</sub> = 1/1/3, GHSV = 3000 h<sup>-1</sup>, P = 0.1 MPa.

## References

---

- (1) Choi, S.; Drese, J. H.; Jones, C. W. *ChemSusChem* **2009**, *2*, 796-854.
- (2) D'Alessandro, D. M.; Smit, B.; Long, J. R. *Angew. Chem., Int. Ed.* **2010**, *49*, 6058-6082.
- (3) Homs, N.; Toyir, J.; Ramírez de La Piscina, P. In *New and Future Developments in Catalysis: Activation of Carbon Dioxide*; (Ed.: S.L. Suib), Elsevier, **2013**, pp. 1-26.
- (4) Boot-Handford, M. E.; Abanades, J. C.; Anthony, E. J.; Blunt, M. J.; Brandani, S.; Mac Dowell, N.; Fernández, J. R.; Ferrari, M.-C.; Gross, R.; Hallett, J. P. *Energy Environ. Sci.* **2014**, *7*, 130-189.
- (5) Daza, Y. A.; Kuhn, J. N. *RSC Adv.* **2016**, *6*, 49675-49691.
- (6) Oyama, S. T. *The chemistry of transition metal carbides and nitrides*, Springer, **1996**, pp. 1-27.
- (7) Hwu, H. H.; Chen, J. G. *Chem. Rev.* **2005**, *105*, 185-212.
- (8) Levy, R.; Boudart, M. *Science* **1973**, *181*, 547-549.
- (9) Rodriguez, J.; Liu, P.; Dvorak, J.; Jirsak, T.; Gomes, J.; Takahashi, Y.; Nakamura, K. *Surf Sci.* **2003**, *543*, L675-L682.
- (10) Viñes, F.; Rodriguez, J. A.; Liu, P.; Illas, F. *J. Catal.* **2008**, *260*, 103-112.
- (11) Patterson, P. M.; Das, T. K.; Davis, B. H. *Appl. Catal. A* **2003**, *251*, 449-455.
- (12) Kunkel, C.; Viñes, F.; Illas, F. *Energy Environ. Sci.* **2016**, *9*, 141-144.
- (13) Posada-Pérez, S.; Viñes, F.; Ramirez, P. J.; Vidal, A. B.; Rodriguez, J. A.; Illas, F. *Phys. Chem. Chem. Phys.* **2014**, *16*, 14912-14921.
- (14) Posada-Pérez, S.; Ramírez, P. J.; Gutiérrez, R. A.; Stacchiola, D. J.; Viñes, F.; Liu, P.; Illas, F.; Rodriguez, J. A. *Catal. Sci. Technol.* **2016**, *6*, 6766-6777.
- (15) Porosoff, M. D.; Kattel, S.; Li, W.; Liu, P.; Chen, J. G. *Chem. Commun.* **2015**, *51*, 6988-6991.
- (16) Wang, T.; Li, Y.-W.; Wang, J.; Beller, M.; Jiao, H. *J. Phys. Chem. C* **2014**, *118*, 8079-8089.

- 
- (17) Li, L.; Sholl, D. S. *ACS Catal.* **2015**, *5*, 5174-5185.
- (18) Tominaga, H.; Nagai, M. *J. Phys. Chem. B* **2005**, *109*, 20415-20423.
- (19) Luo, Q.; Wang, T.; Walther, G.; Beller, M.; Jiao, H. *J. Power Sources* 2014, **246**, 548-555.
- (20) Shi, Y.; Yang, Y.; Li, Y. W.; Jiao, H. *Appl. Catal. A* 2016, **524**, 223-236
- (21) Porosoff, M. D.; Yang, X.; Boscoboinik, J. A.; Chen, J. G. *Angew. Chem., Int. Ed.* **2014**, *126*, 6823-6827.
- (22) Giordano, C.; Erpen, C.; Yao, W.; Antonietti, M. *Nano Lett.* **2008**, *8*, 4659-4663.
- (23) Kresse, G.; Furthmüller, J. *Phys. Rev. B* **1996**, *54*, 11169.
- (24) Perdew, J. P.; Burke, K.; Ernzerhof, M. *Phys. Rev. Lett.* **1996**, *77*, 3865-3868.
- (25) Grimme, S.; Antony, J.; Ehrlich, S.; Krieg, H. *J. Chem. Phys.* **2010**, *132*, 154104.
- (26) Shi, X.-R.; Wang, S.-G.; Wang, H.; Deng, C.-M.; Qin, Z.; Wang, J. *Surf. Sci.* **2009**, *603*, 852-859.
- (27) Wang, T.; Liu, X.; Wang, S.; Huo, C.; Li, Y.-W.; Wang, J.; Jiao, H. *J. Phys. Chem. C* **2011**, *115*, 22360-22368.
- (28) Wang, T.; Wang, S.; Li, Y.-W.; Wang, J.; Jiao, H. *J. Phys. Chem. C* **2012**, *116*, 6340-6348.
- (29) Wu, W.; Wu, Z.; Liang, C.; Chen, X.; Ying, P.; Li, C. *J. Phys. Chem. B* **2003**, *107*, 7088-7094.
- (30) Wu, W.; Wu, Z.; Liang, C.; Ying, P.; Feng, Z.; Li, C. *Phys. Chem. Chem. Phys.* **2004**, *6*, 5603-5608.
- (31) Dieterle, M.; Mestl, G. *Phys. Chem. Chem. Phys.* **2002**, *4*, 822-826.
- (32) Oshikawa, K.; Nagai, M.; Omi, S. *J. Phys. Chem. B* **2001**, *105*, 9124-9131.
- (33) Gao, Q.; Zhao, X.; Xiao, Y.; Zhao, D.; Cao, M. *Nanoscale* **2014**, *6*, 6151-6157.
- (34) Sun, Y.; Hu, X.; Luo, W.; Huang, Y. *J. Mater. Chem.* **2012**, *22*, 425-431.

- 
- (35) Zhu, Y.; Wang, S.; Zhong, Y.; Cai, R.; Li, L.; Shao, Z. *J. Power Sources* **2016**, *307*, 552-560.
- (36) Bhaskar, A.; Deepa, M.; Narasinga Rao, T. *ACS Appl. Mater. Interfaces* **2013**, *5*, 2555-2566.
- (37) Chen, M.; Liu, J.; Zhou, W.; Lin, J.; Shen, Z. *Sci. Rep.* **2015**, *5*, 10389.
- (38) Li, R.; Wang, S.; Wang, W.; Cao, M. *Phys. Chem. Chem. Phys.* **2015**, *17*, 24803-24809.
- (39) Wang, G.; Schaidle, J. A.; Katz, M. B.; Li, Y.; Pan, X.; Thompson, L. T. *J. Catal.* **2013**, *304*, 92-99.
- (40) Arnoldy, P.; De Jonge, J. C. M.; Moulijn, J. A. *J. Phys. Chem.* **1985**, *89*, 4517-4526.
- (41) Han, J. W.; Li, L.; Sholl, D. S. *J. Phys. Chem. C* **2011**, *115*, 6870-6876.
- (42) Shou, H.; Li, L.; Ferrari, D.; Sholl, D. S.; Davis, R. J. *J. Catal.* **2013**, *299*, 150-161
- (43) Shi, X.-R.; Wang, J.; Hermann, K. *J. Phys. Chem. C* **2010**, *114*, 13630-13641.
- (44) Liu, P.; Rodriguez, J.A. *J. Phys. Chem. B*, **2006**, *110*, 19418-19425.
- (45) Medford, A. J.; Vojdovic, A.; Studt, F.; Abild-Pedersen, F.; Nørskov, J. K. *J. Catal.* **2012**, *290*, 108-117.
- (46) Shi, X.-R.; Wang, S.-G.; Hu, J.; Qin, Z.; Wang, J. *Surf. Sci.* **2012**, *606*, 1187-1194.
- (47) Tokarz-Sobieraj, R.; Gryboś, R.; Witko, M. *Appl. Catal. A* **2011**, *391*, 137-143.
- (48) Raskó, R.; Kiss, J. *Appl. Catal. A* **2003**, *253*, 427-436.
- (49) Davydov, A. A.; Shepot'ko, M. L. *Theor. Exp. Chem.* **1991**, *26*, 449-455.
- (50) Tait, S. L.; Dohnálek, Z.; Campbell, C. T.; Kay, B. D. *J. Chem. Phys.* **2006**, *125*, 234308.
- (51) Wang, C.-C.; Wu, J.-Y.; Jiang, J.-C. *J. Phys. Chem. C* **2013**, *117*, 6136-6142.
- (52) Smith, R. S.; Li, Z.; Dohnálek, Z.; Kay, B. D. *J. Phys. Chem. C* **2014**, *118*, 29091-29100.

---

(53) Reuter K.; Scheffler M. *Phys. Rev. B* **2001**, *65*, 035406.